Observations of Water Mass Transformation and Eddies in the Lofoten Basin of the Nordic Seas

CLARK G. RICHARDS* AND FIAMMETTA STRANEO

Woods Hole Oceanographic Institution, Woods Hole, Massachusetts

(Manuscript received 1 December 2014, in final form 8 April 2015)

ABSTRACT

The Lofoten basin of the Nordic Seas is recognized as a crucial component of the meridional overturning circulation in the North Atlantic because of the large horizontal extent of Atlantic Water and winter surface buoyancy loss. In this study, hydrographic and current measurements collected from a mooring deployed in the Lofoten basin from July 2010 to September 2012 are used to describe water mass transformation and the mesoscale eddy field. Winter mixed layer depths (MLDs) are observed to reach approximately 400 m, with larger MLDs and denser properties resulting from the colder 2010 winter. A heat budget of the upper water column requires lateral input, which balances the net annual heat loss of $\sim$80 W m^{-2}. The lateral flux is a result of mesoscale eddies, which dominate the velocity variability. Eddy velocities are enhanced in the upper 1000 m, with a barotropic component that reaches the bottom. Detailed examination of two eddies, from April and August 2012, highlights the variability of the eddy field and eddy properties. Temperature and salinity properties of the April eddy suggest that it originated from the slope current but was ventilated by surface fluxes. The properties within the eddy were similar to those of the mode water, indicating that convection within the eddies may make an important contribution to water mass transformation. A rough estimate of eddy flux per unit boundary current length suggests that fluxes in the Lofoten basin are larger than in the Labrador Sea because of the enhanced boundary current–interior density difference.

1. Introduction

The meridional overturning circulation (MOC) constitutes a major pathway through which heat input to the ocean in the tropics is moved poleward. The subsequent densification and sinking of warm surface waters at high latitudes due to surface fluxes feeds the return branch of the MOC, whereby deep, dense currents fill the ocean basins and remain isolated from the atmosphere until being mixed back to the surface. An understanding of the dynamics of the MOC is crucial for constructing a complete picture of the current climate of the planet as well as understanding past climate shifts and predicting future changes (both natural and anthropogenic).

It has been known for some time that the formation of dense water at high latitudes is limited to a few key regions, notably the Southern Ocean (in the Southern Hemisphere) and the Labrador, Irminger, and Nordic Seas (in the Northern Hemisphere). In the North Atlantic, the classic view of deep convection resulting from water mass transformation occurring only in a few isolated regions (e.g., the Labrador and Greenland Seas) has shifted to include densification occurring along the pathways of warm-water inflow (e.g., Mauritzen 1996a,b; Isachsen et al. 2007). Further, the role of eddies shed by the warm-water boundary currents has also emerged as a key factor in the water mass modification and subsequent restratification, as seen in observations in the Labrador Sea (Lilly et al. 2003; Chanut et al. 2008; de Jong et al. 2013) as well as models (Spall 2005; Deshayes et al. 2009; Gelderloos et al. 2011; Straneo 2006a,b).

Within the Nordic Seas, the role played by the Lofoten basin (see Fig. 1) in the transformation of Atlantic Water (AW) is increasingly being recognized (Isachsen et al. 2007; Rossby et al. 2009a). Situated between two branches of the inflowing current, the Lofoten basin exhibits the deepest AW layer of the entire Nordic Seas. This deep layer is indicative of a large pool of warm–salty water, resulting in large surface buoyancy losses (Rossby et al. 2009b,a), with efficient export of the transformed water by the mean AW currents (Søiland

* Current affiliation: RBR Ltd., Ottawa, Ontario, Canada.

Corresponding author address: Clark G. Richards, 95 Hines Rd., Unit 5, Ottawa ON K2K 2M5 Canada.
E-mail: clark.richards@rbr-global.com

DOI: 10.1175/JPO-D-14-0238.1

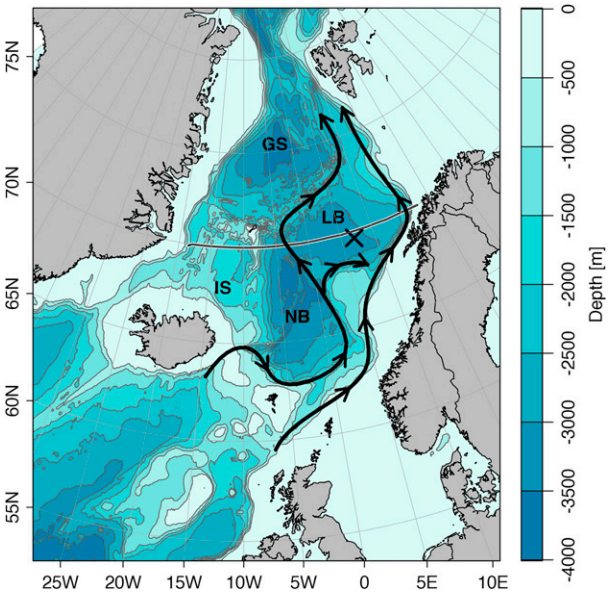

FIG. 1. Map of the Nordic Seas, showing bathymetry and the location of the Lofoten basin mooring (×). The four major basins are identified as the Norwegian basin (NB), Lofoten basin (LB), Greenland Sea (GS), and Iceland Sea (IS). The arrows indicate the approximate locations of the two branches of Atlantic Water inflow to the Nordic Seas. The line at 70°N indicates the section plotted in Fig. 3.

et al. 2008). The mechanism by which this pool of AW is maintained has been attributed to anticyclones shed from the inner branch of the northward-flowing current, where the shelf topography is steepest (Köhl 2007; Spall 2010; Rossby et al. 2009b; Volkov et al. 2013). These anticyclones drift westward in the basin, where they are trapped by the closed geostrophic contours. This view is supported by model simulations and by remote sensing and drifter datasets (Köhl 2007; Isachsen et al. 2012). To date, however, there have been no direct observations of the water mass transformation process, the vertical structure of the eddies, or of their contribution to the lateral heat–salt flux in the Lofoten basin. Through these lateral fluxes, the narrow boundary current is transformed into a broad region over which surface buoyancy losses are maximized (Spall 2011). Studies of the Nordic Seas have made use of rich but sparsely sampled hydrography (e.g., Nilsen and Falck 2006; Rossby et al. 2009a; Mork et al. 2014), surface altimetry (Volkov et al. 2013), drifters (Andersson et al. 2011; Poulain et al. 1996; Koszalka et al. 2013; Rossby et al. 2009b; Voet et al. 2010), and numerical models (Köhl 2007; Spall 2010; Isachsen et al. 2012). High temporal resolution measurements of the vertical structure of hydrography and currents are currently lacking.

The goal of the present study is to fill this gap by describing the water mass transformation and mesoscale eddy properties using observations. In section 2, we describe the data and processing used in the study, including the mooring data, atmospheric reanalysis, and climatological hydrography. Section 3 will explore the role of the Lofoten basin within the Nordic Seas from the perspective of the climatological fields as well as the evolution of the wintertime mixed layer properties and a one-dimensional heat budget. Section 4 will examine the eddy field observed by the mooring, followed by a discussion in section 5 and a summary of results in section 6.

2. Data

a. Mooring

In situ data were collected with an instrumented mooring, deployed from July 2010 to September 2012 (at 69°39.18′N, 6°57.42′E; see Fig. 1), with a turnaround in May 2011. The mooring location was chosen to be in the region of high eddy kinetic energy that spreads out from the boundary current (e.g., Köhl 2007), to be able to sample passing eddies as well as properties of the interior basin. The location was also chosen to be to the east of the large semipermanent anticyclone (see section 3a). The initial deployment in 2010 consisted of a McLane Moored Profiler (MMP), executing profiles between the 100- and 900-m depths approximately every 16 h. The MMP contained a CTD and an acoustic current meter, the latter of which malfunctioned. Above the MMP, attached to the flotation sphere at ~100 m, was a Seabird MicroCAT (measuring conductivity, temperature, and pressure) and an upward-looking 300-kHz RD Instruments (RDI) acoustic Doppler current profiler (ADCP). The 2010 mooring also contained MicroCATs mounted at the 902-, 1000-, 1250-, and 2500-m depths, as well as an acoustic current meter (Nortek Aquadopp) at 2500 m (a second Aquadopp at 902 m flooded).

In addition to the failure of the MMP current meter, the MMP itself suffered a leak in one of its flotation spheres, resulting in fewer full depth range profiles through time. The loss of data is worst from December 2010 to May 2011, at which point the mooring was turned around.

On turnaround, the profiler was replaced with a series of fixed-depth MicroCATs at 50, 100, 150, 200, 300, 400, 500, 750, 900, 1000, 1250, and 2500 m. The MicroCATs at 150, 200, 300, 500, 750, 900, 1250, and 2500 m were paired with Aquadopp current meters. The 2011 mooring also contained an upward-looking ADCP mounted to the sphere at 100 m. Data return from the instruments on the 2011 mooring was 100%.

Processing of the MicroCAT data involved despiking the measured time series (both manually for large spikes

and using a running median filter) and then calculating salinity from the measured conductivity, temperature, and pressure. Several of the MicroCATs exhibited time-varying salinity offsets (i.e., step changes), which were corrected based on observed temperature and salinity properties before and after the offset occurred. Aquadopp processing involved simply rotating the measured u and v velocities for the local magnetic declination of ~3.5°W, while ADCP processing involved both the declination correction and mapping range bins to depth bins based on the measured pressure.

Processing of the MMP CTD profiles involved despiking anomalous salinity measurements and manual correction of time-varying offsets similarly to the MicroCAT data processing. The salinity calibrations for the MMP and MicroCATs were checked against ship CTD profiles collected before deployment and after recovery during both 2010 and 2011; however, uncertainty in the CTD calibration lead to a final accuracy of the mooring salinity of about 0.01.

b. *Reanalysis and ocean climatology*

Historical reanalysis data used for the surface fields were obtained from the ERA-Interim dataset (Dee et al. 2011). The 6-hourly analysis (surface pressure, sea surface temperature, etc.) and forecast (precipitation, evaporation, surface fluxes, etc.) fields were obtained for the years 2010–12. Monthly averages of the same fields were obtained for the years 1979–2012, used for calculating climatological values.

Climatological hydrographic fields were obtained from the *World Ocean Atlas* (*WOA*) Greenland, Iceland, and Norwegian Seas (GINS) climatology (Seidov et al. 2014). Climatological temperature and salinity are provided at standard *WOA* depths on an objectively analyzed 0.1° grid for monthly, seasonal, and annually averaged time scales.

3. Water mass transformation in the Lofoten basin

a. *Physical setting and Atlantic Water distribution*

The Nordic Seas (comprising the Greenland, Iceland, and Norwegian Seas) lie between Greenland and Norway, north of the Greenland–Scotland Ridge and south of the Arctic Ocean, which is connected via the Fram Strait (Fig. 1). North of Norway, the Nordic Seas open eastward into the Barents Sea, a shallow shelf sea connected to the Arctic Ocean. Schematically, the Nordic Seas can be divided by bathymetric features into four basins: the Norwegian and Lofoten basins to the east (which make up the Norwegian Sea) and the Greenland and Iceland Seas to the west (Fig. 1).

Relatively warm and salty Atlantic Water enters the Nordic Seas between the Faroe–Scotland Channel, to the north of the Faroe Islands and to the west of Iceland (e.g., Hansen and Østerhus 2000; Orvik et al. 2001; Rossby et al. 2009b). Upon entering the Nordic Seas, the AW flows poleward along two main branches: the inner and outer branches of the Norwegian Atlantic Current (NwAC; see Fig. 1). The inner branch follows the continental slope along the Norwegian shelf, while the outer branch is a less well-defined baroclinic current that follows topography along the westernmost extent of the boundary between the warm–salty AW and the cool–fresh waters occupying the Greenland and Iceland Seas (see, e.g., Mork and Skagseth 2010).

In the Lofoten basin, the horizontal extent of AW is observed to be larger than anywhere else in the Nordic Seas, as can be seen by the climatological depths of the 3°C and 35.0 psu isosurfaces (Fig. 2). The climatological AW layer in the basin reaches depths >700 m. Further, the extent to which the warm–salty AW is confined to the closed topographic contours of the Lofoten basin is striking, even for the annually averaged climatology. The persistence of such a warm-water mass throughout the year in the Lofoten basin has a significant effect on air–sea fluxes and densification of the poleward-flowing AW. The location of deepest AW extent is found in the center of the Lofoten basin, some 500 km from the slope where the main current flows. The deep AW extent is likely the signature of a semipermanent anticyclonic eddy, known as the Lofoten vortex (see, e.g., Köhl 2007; Rossby et al. 2009a; Søiland and Rossby 2013). The origin of the vortex, while still poorly understood, is hypothesized to result from the merger of warm–salty anticyclonic eddies shed from the boundary current along the Norwegian continental slope (Köhl 2007). While the Lofoten vortex is an interesting dynamical feature and may potentially be relevant to the basin as a whole, its role in the transformation process within the Lofoten basin is still unclear and it is not the focus of the current study. The shoaling of the isotherms and isohalines toward the eastern Lofoten basin observed in the climatology was interpreted by Rossby et al. (2009a) to be indicative of a connection between the deep pool of AW and the slope current.

The horizontal and vertical spreading of AW in the Lofoten basin can also be seen in synoptic sections, an example of which is shown in Fig. 3, a hydrographic section taken during June 2002 along 70°N (Jeansson et al. 2008). The warm–salty AW layer overlies cold–fresh water sourced from the western portion of the Nordic Seas. The highest temperatures and salinities are found in the slope boundary current (i.e., the inner branch of the NwAC; see the insets in Fig. 3), representing the most

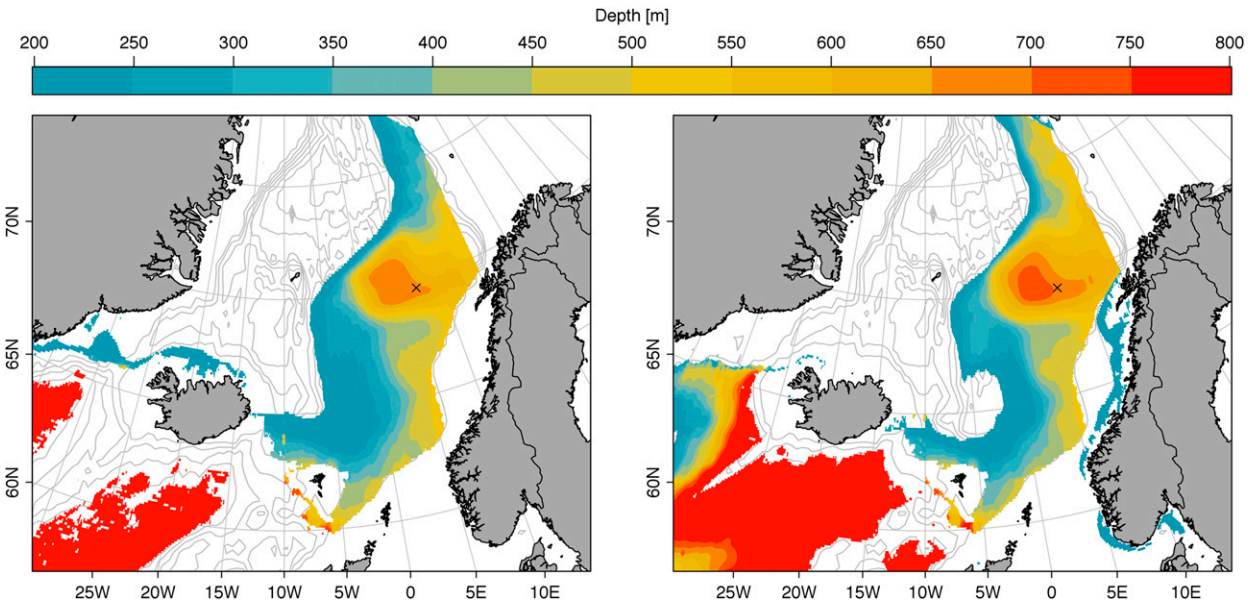

FIG. 2. Horizontal spreading of Atlantic Water in the Nordic Seas. (a) Depth of the 3°C isotherm, and (b) depth of the 35.0 psu isohaline. From the *WOA* GINS $^1/_{10}°$ climatology (Seidov et al. 2013). The mooring location is indicated by the ×.

likely source of redistributed AW in the Lofoten basin. Also apparent in the section around 3°E is the signature of the Lofoten vortex, which causes a deepening of the AW layer to >1000 m and nearly uniform temperature and salinity profiles from the surface to 1000-m depth, typical of other observations within the eddy (e.g., Søiland and Rossby 2013).

b. *Air–sea fluxes*

The lateral spreading of AW in the Lofoten basin should have a signature in the climatological surface buoyancy fluxes of the Nordic Seas. The flux of buoyancy at the ocean surface can be written as a sum of thermal and saline forcings as (e.g., Gill 1982; Martin and Moore 2007)

$$B = \frac{g\alpha}{\rho_0 C_p}(Q_s + Q_l + Q_R) + \frac{g\beta S}{\rho_0}(P - E), \qquad (1)$$

where g is the acceleration due to gravity, α and β are the thermal and haline expansion coefficients for seawater, S is the surface salinity, ρ_0 is a reference density, and $C_p(S, T, p)$ is the specific heat for seawater. The terms Q_s, Q_l, and Q_R are the sensible, latent, and net radiative heat fluxes (Q_R is the sum of the net longwave radiation Q_{lw} and the net shortwave radiation Q_{sw} at the surface), and P and E are the precipitation and evaporation, respectively. All variables are defined to be positive downward—a positive buoyancy flux implies an increase in the buoyancy (decrease of density) of surface waters. Note that Eq. (1) describes changes in surface buoyancy flux due to atmospheric processes and does not include terms due to oceanic processes (e.g., melting of ice in the East Greenland Current).

Annually averaged 1979–2012 surface buoyancy fluxes, plotted in Fig. 4a, highlight the effect of the warm AW inflow and lateral spreading over the Lofoten basin, with the largest negative fluxes observed over the eastern Nordic Seas. Overall, the climatological patterns of surface buoyancy flux over the Nordic Seas correlate with the climatological ocean surface temperature (not shown), owing to the dominance of the heat flux terms over precipitation and evaporation in Eq. (1). On average, the contribution of the heat flux to the total buoyancy flux is about 7 times that of the salt flux over the Nordic Seas. The region of reduced surface buoyancy flux over the Iceland Sea extending toward the Norwegian basin has been described by Moore et al. (2012).

The Lofoten basin experiences larger wintertime (December, January, and February) surface buoyancy loss than any of the other basins, with a mean wintertime buoyancy flux of $-5.99 \pm 0.66 \times 10^{-8}\,\mathrm{m^2\,s^{-3}}$ compared to $-3.75 \pm 0.50 \times 10^{-8}\,\mathrm{m^2\,s^{-3}}$ over the entire Nordic Seas (Fig. 4b, where the ± indicates the standard deviation). Integrated over the climatological winter season, the Lofoten basin alone accounts for over $^1/_3$ of the total buoyancy loss over the Nordic Seas even though it only covers $^1/_5$ of the total area.

c. *Evolution of water column temperature and salinity*

The large wintertime surface buoyancy losses in the Lofoten basin are expected to have a significant effect on

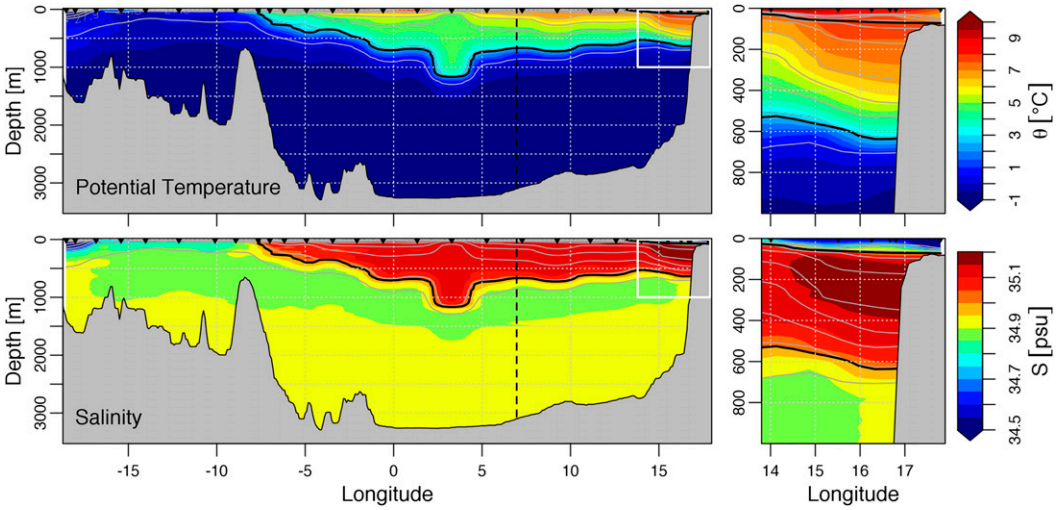

FIG. 3. (top) Potential temperature and (bottom) salinity sections across the Nordic Seas along 70°N, from the R/V *Knorr* cruise 166 Leg 11, June 2002 (Jeansson et al. 2008). The solid black contour indicates the $S = 35.0$ psu isohaline, and the panels on the right show a close up of the region in the white box. Locations of CTD stations are indicated by the inverted triangles. Isopycnals are shown as gray lines, with a contour interval of 0.1 kg m^{-3}. The vertical dashed line indicates the mooring location.

the water column properties as observed by the mooring. The wintertime modification of AW in the Lofoten basin, the product of which will ultimately continue northward, is therefore important to the overall production of dense overflows that feed the MOC. In this section, we examine the observed water column properties, focusing on the winter months during which the surface buoyancy losses contribute to a deepening mixed layer and the creation of a mode-water product.

1) MIXED LAYER DEPTH

The mixed layer is a region of the upper water column within which salinity, temperature, and density are nearly uniform. It results from interaction with the atmosphere, through downward turbulent mixing induced by wind stress and surface density changes. Determination of the mixed layer depth (MLD) has long been of interest in oceanography, as it strongly influences the upper-ocean heat content and mechanical inertia that is interacting with the atmosphere (e.g., de Boyer Montégut et al. 2004; Pickard and Emery 1990).

Definitions of what constitutes the mixed layer vary between studies, depending on the type and vertical resolution of the data used. Kara et al. (2000, hereinafter KRH) summarize a variety of studies that used either temperature or density criteria for finding the MLD [or isothermal layer depth (ILD)] and define an optimal method for use with coarse-resolution datasets, such as climatologies or ocean general circulation models. The MLD method proposed by KRH interpolates to find the depth at which the density has increased from a near-surface reference value by $\Delta\sigma_t$. The authors define the density difference based on a temperature difference ΔT as

$$\Delta\sigma_t = \sigma_t(T + \Delta T, S, p) - \sigma_t(T, S, p), \qquad (2)$$

where T, S, and p are the surface temperature, salinity, and pressure (with $p = 0$ at the surface), and ΔT is the temperature difference from the surface value. KRH suggest that $\Delta T = 0.8$°C is a reasonable value for the global ocean, though they acknowledge that there will likely be some seasonal and geographical variability. In situations where high vertical resolution data are available, a density gradient criterion (where $\partial\sigma_t/\partial z$ or $\partial T/\partial z$ exceeds a threshold value) may be used to identify the base of the mixed layer (e.g., Brainerd and Gregg 1995).

As the mooring data differed between the 2 yr, particularly in the vertical resolution of measurements, the choice of an optimal MLD definition is ambiguous. To facilitate comparison of the MLDs between the 2 yr, the density difference criterion of KRH, using $\Delta T = 0.2$°C was chosen, which was justified by comparing against "exact" MLDs as assessed from the MMP on the 2010 mooring when possible. A detailed description of the method and the comparison between approaches is given in the appendix.

A time series of smoothed MLD for winter 2010 (December 2010 to April 2011) and 2011 (December 2011 to April 2012) is shown in Fig. 5, plotted with both density and stratification fields gridded from the

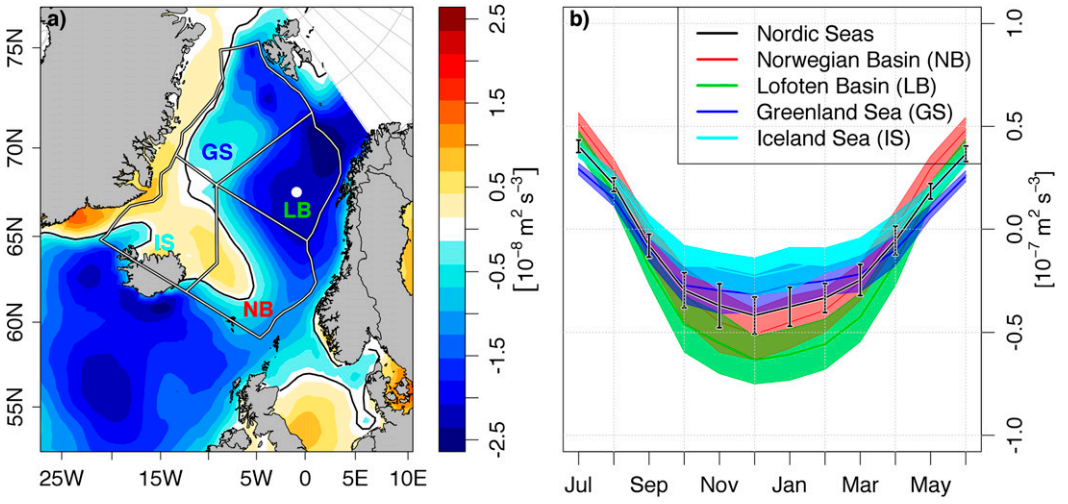

FIG. 4. Surface buoyancy flux ($m^2 s^{-3}$) for the Nordic Seas. (a) Mean buoyancy flux, calculated using ERA-Interim fields from 1979 to 2012, and (b) monthly mean, area-averaged buoyancy fluxes for each of the basins in the Nordic Seas. Shaded regions in (b) indicate the standard deviation of the averages. The white circle indicates the location of the mooring.

mooring data. MLDs for 2010 were generally deeper than 2011; however, both series exhibit significant variability over time scales of several weeks. This variability likely reflects both the variability in air–sea interaction (e.g., passing storms; as in Isachsen et al. 2013) and mesoscale eddy activity (e.g., Köhl 2007).

2) MIXED LAYER PROPERTIES

In 2010, the deepening of the mixed layer was already underway by November, where it was estimated to be already deeper than the 100-m MicroCAT. The deepening continues almost linearly until about March, reaching a maximum depth of about 450 m, after which restratification begins. It should be noted that the MLD estimates toward the end of the 2010 record are the most uncertain due to the lack of MMP profiles, and it is likely that the restratification is captured by the KRH method only approximately. By the end of April 2010, the water column has restratified to at least the depth of the 100-m MicroCAT.

In 2011, the mixed layer begins deepening later than in 2010, with a clear increase beginning in early December. Deepening continues until it reaches about 200 m in January 2012 and afterward fluctuates around this depth until restratification begins in late April 2012. The deepest mixed layer event occurs in April 2012 and coincides with a large deepening of the AW layer, as seen in the depth of the 35.0 psu isohaline (Fig. 5a).

Figure 5b highlights the changes in stratification that occur as a result of the winter mixed layer deepening. Note that the deep pycnocline (~700 m), which coincides with the 35.0 isohaline and indicates the base of the AW layer, provides a maximum depth for the surface-forced convection and persists throughout the entire record. The deep pycnocline also experiences significant vertical variability, most likely related to mesoscale heaving. Near the surface, the upper pycnocline deepens in winter as convection homogenizes the upper water column through surface buoyancy loss. Upper-layer stratification is mostly eroded by February in both years. Restratification occurs around April/May, at which point the near-surface pycnocline is reestablished and the MLD rises beyond the uppermost MicroCATs.

The average winter mixed layer water column properties (e.g., temperature, salinity, and density) can be estimated for both 2010 and 2011. The 2010 and 2011 mixed layer properties are summarized in a potential temperature–salinity (TS) plot in Figs. 6b and 6d, alongside TS plots showing the monthly curves of water column properties from the two separate mooring deployments (Figs. 6a,c). The mixed layer evolution differs slightly between the 2 yr, with an overall saltier mixed layer in 2010 (by ~0.04 psu). Mixed layers in both years exhibit a trajectory in TS space that shows a marked decrease in temperature (by about 2°–3°C) during the early part of the winter, with an initial increase in salinity followed by a slight decrease as the mixed layer deepens (~0.05 in 2010 and ~0.02 in 2011).

The mixed layer salinity variations are likely caused by a combination of entrainment from below as the mixed layer deepens, lateral transport of coastal freshwater in the surface layer by winds, and variations in surface forcing of $P - E$. At Ocean Weather Station M (OWSM; in the central Norwegian Sea), average winter mixed layer salinity was observed to increase through fall and winter, with a maximum around May (Nilsen

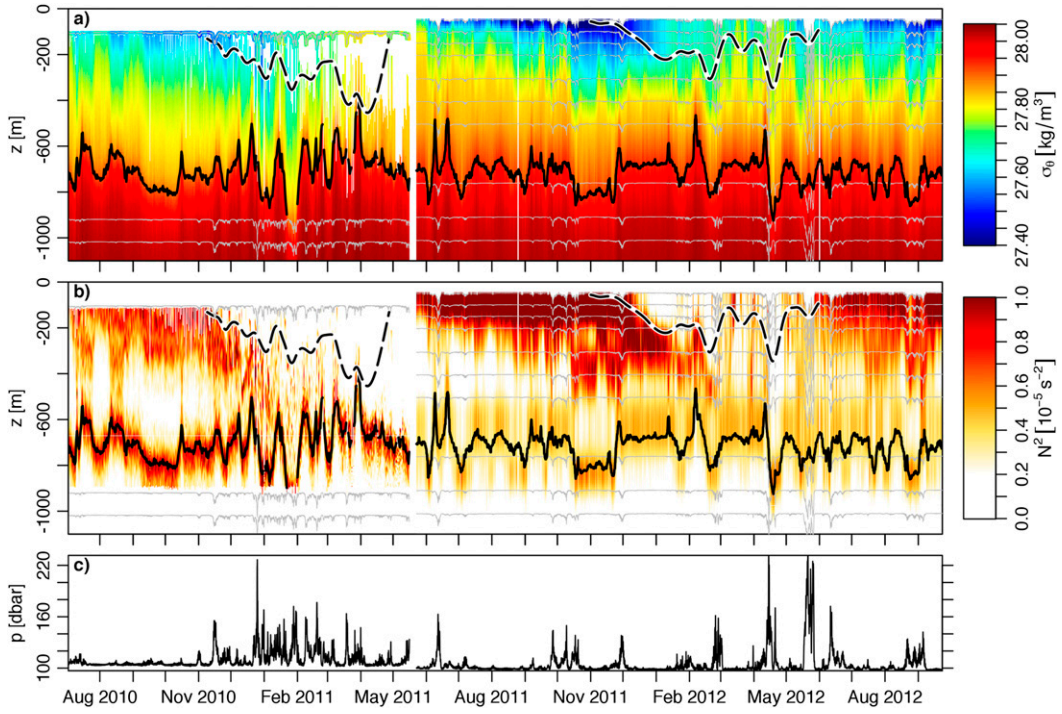

FIG. 5. Winter MLD estimates for 2010 and 2011. The MLD (dashed line) and depth of the 35.0 psu isohaline (solid line) are plotted over (a) potential density and (b) squared buoyancy frequency. The 2 yr are combined to highlight the differences in vertical sampling. For 2010, the individual MMP profiles are shown (with gaps) along with time series of the MicroCAT at 100 m. The MicroCAT fields located below the MMP have been gridded with the MMP profiles. For 2011, the fixed-depth MicroCATs have been interpolated between instruments. The gray lines show the depths of the MicroCATs. (c) The pressure as measured by the MicroCAT at 100 m.

and Falck 2006). In winter 2010, estimates of $P - E$ for the mooring location from the ERA reanalysis indicate that the mixed layer salinity should increase by about 0.01, suggesting that there must be lateral transport of freshwater near the surface not captured by the mooring because there are no instruments shallower than 50 m. In winter 2011, the $P - E$ contribution is opposite (i.e., P exceeds E) and predicts a salinity decrease of ~0.02, consistent with the observations. In 2010, the mixed layer salinity decrease produces a final salinity that is similar to the salinity of the 2011 mixed layer, though with a larger final density. The highest mixed layer densities occur with the largest MLDs (colors of points in Figs. 6b,d).

The density of the end product of the winter convection period is estimated by the maximum density of the winter mixed layer, indicated in Figs. 6b and 6d by the solid black isopycnal. The maximum mixed layer densities were observed to be 27.85 and 27.79 kg m^{-3} for winter 2010 and 2011, respectively. It is worth noting that the minimum density of Denmark Strait overflow waters is approximately 27.8 kg m^{-3} (see, e.g., Hansen and Østerhus 2000) and that the product of water mass transformation in the Lofoten basin is similar.

The variation in the evolution of MLD between 2010 and 2011 are primarily caused by variations in the seasonal buoyancy flux, which as stated previously is dominated by heat flux. Mean winter/spring buoyancy fluxes (October–April) for 2010 and 2011 correspond to -5.63×10^{-8} and -4.82×10^{-8} m^2 s^{-3}, respectively. In addition to the larger winter buoyancy flux in 2010, the large, negative fluxes began earlier than in 2011. This can be seen by comparing the time series of buoyancy flux for the two winter seasons (Fig. 7) as well as by the earlier deepening of the mixed layer in 2010 (Fig. 5).

d. *Upper-ocean heat content*

In this section, we investigate the extent to which the transformation of waters at the mooring location can be attributed to surface fluxes. Because of the lack of measurements from the MMP in the 2010 deployment, it is not possible to accurately estimate the water column heat content at the mooring location during that period. In this section, because of data availability, we focus only on the measurements made during the 2011 deployment.

Water column heat content change relative to an initial time $t = t_0$ in a layer between depths z_1 and z_2 was

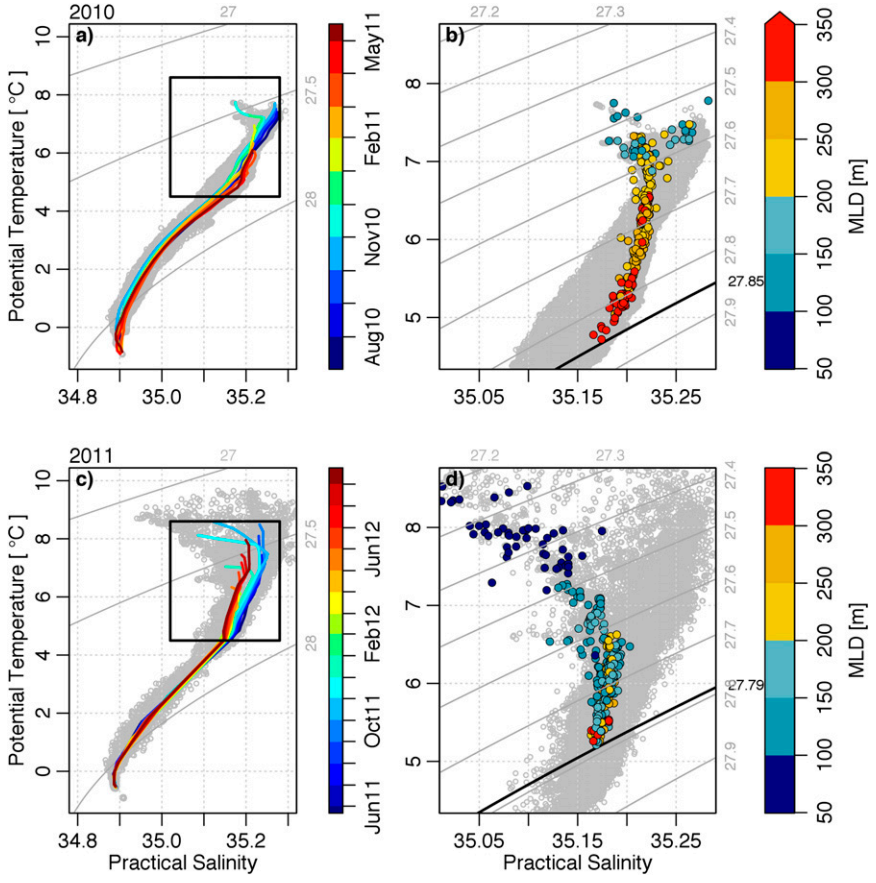

FIG. 6. The 2010 and 2011 mixed layer properties. (a),(c) Monthly average TS profiles, and (b),(d) winter mixed layer temperature and salinity for 2010 and 2011. In (b) and (d), the points are colored for the MLD. In each plot, the gray dots show the θ and S values of all points measured by the mooring. The boxes in (a) and (c) indicate the limits of the plot in (b) and (d).

estimated through vertical integration of the temperature profile:

$$\Delta \mathrm{HC}(t) = \rho C_p \int_{z_1}^{z_2} T(t,z) - T(t_0,z)\, dz \qquad (3)$$

(see, e.g., Davis et al. 2013; Skagseth and Mork 2012). Heat content input to the water column through the surface heat flux was calculated by integrating the ERA-Interim net heat flux Q_{net} in time according to

$$\mathrm{HC}_{Q_{\mathrm{net}}}(t) = \int_{t_0}^{t} Q_{\mathrm{net}}(t)\, dt. \qquad (4)$$

Heat input through vertical mixing at the base of the layer is assumed to be negligible compared to the surface fluxes.

In the absence of lateral transport of heat, there should exist a balance between changes in water column heat content and input from surface fluxes, provided z_2 is deeper than the maximum MLD. Any imbalance between these two fields indicates a contribution from lateral fluxes, which, given the present dataset (i.e., an Eulerian measurement), cannot be evaluated by any other method.

It is assumed that only the upper portion of the water column will be influenced by surface fluxes, with the deepest MLD representing the limit of atmospheric influence. The heat content change (calculated relative to the heat content at the beginning of the 2011 mooring deployment) over the upper 500 m was calculated from Eq. (3) and compared with the heat content change expected from the surface fluxes from Eq. (4) (Fig. 8). The lateral contribution of heat, inferred from the difference between heat content change and the atmospheric forcing, increases nearly linearly over the 16 months that the mooring was deployed. It is clear from Fig. 8 that a lateral influx of heat is required to balance the net heat loss to the atmosphere (e.g., section 3b).

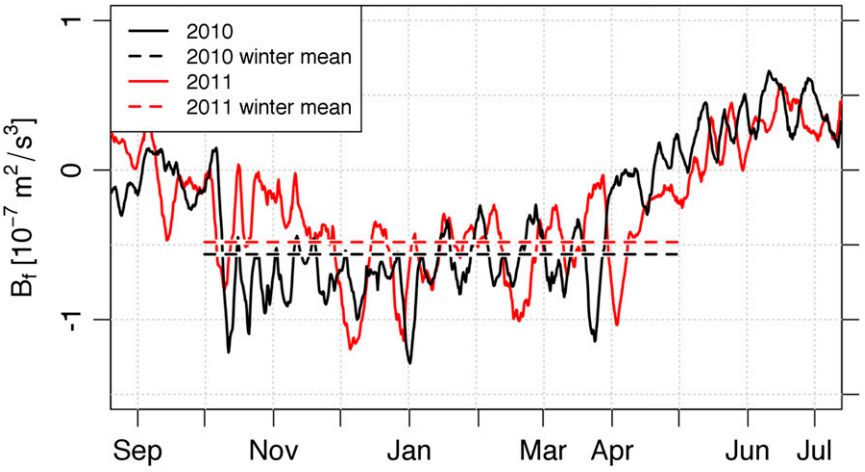

FIG. 7. Time series of buoyancy flux from ERA-Interim at the mooring location smoothed with a 5-day boxcar filter for 2010 (black line) and 2011 (red line). Mean winter buoyancy fluxes for 2010 and 2011 are indicated by the dashed horizontal lines.

To compare the observed heat content changes with what would be expected based on the climatological values, identical fields were calculated using both the GINS climatology and the ERA-Interim fields. The results, including the inferred lateral contribution to heat content change to the upper 500 m, are indicated by the dashed lines in Fig. 8. Even though the surface flux contribution through summer 2011 was higher and peaked later than the climatological fluxes, the winter minimum was also larger. The result is that both the observed heat content changes and the inferred lateral contribution agree relatively well with the climatological estimates.

The origin of the lateral contribution of heat in the Lofoten basin cannot be unambiguously identified based on the mooring measurements. If the mean flow into the basin from the NwAC is small (see, e.g., Søiland et al. 2008; Voet et al. 2010), the lateral fluxes can be assumed to result from the propagation of AW eddies shed from the boundary current along the Lofoten slope (Köhl 2007; Spall 2010). The green curves in Fig. 8 suggest that at the mooring location the lateral addition of heat is relatively constant throughout the year—in both the 2011/12 time series and from the climatology—and a straight line fit gives a lateral heat flux of about 80 $W m^{-2}$. This is consistent with previous estimates of the annually averaged heat flux in the Lofoten basin (Isachsen et al. 2007).

Previous hypotheses relating the magnitude of the eddy activity in the Lofoten basin to the seasonal strength of the boundary current (e.g., faster flows in winter result in more vigorous instabilities in the current) are not reflected in the observed heat content changes. It should be kept in mind that the mooring location was chosen to be outside of the main region of boundary current instability and thus a seasonal signal of eddy activity may be masked by the accumulation and propagation of eddies within the basin, which are spread over a larger region as they propagate cyclonically around the Lofoten basin (see, e.g., Volkov et al. 2013).

Overall, changes in surface heat content in the Lofoten basin require a lateral input of heat to balance atmospheric fluxes. This lateral advection is most likely the result of eddy heat fluxes, and it has a consistent signature in climatological values. To better understand water mass transformation and the heat–salt budget of the Lofoten basin, the next section will examine characteristics of the eddies as observed by the mooring.

4. Eddies

Previous studies of boundary current–sourced eddies in high-latitude seas have highlighted both the importance of the eddies on the seasonal cycle of convection and restratification and the difficulties in obtaining high-resolution measurements of such eddies. In the Labrador Sea, warm and salty anticyclones sourced from the Irminger Current (IC) are a direct source of heat and salt, particularly in spring following convection events (Lilly et al. 1999, 2003; Rykova et al. 2009; de Jong et al. 2013). These so-called Irminger rings result from instabilities in the Irminger Current along the west coast of Greenland and have a distinctive signature in altimetric maps of sea level anomaly (de Jong et al. 2013). Similar processes and eddies have been observed in the Irminger Sea, where anticyclones have been observed to

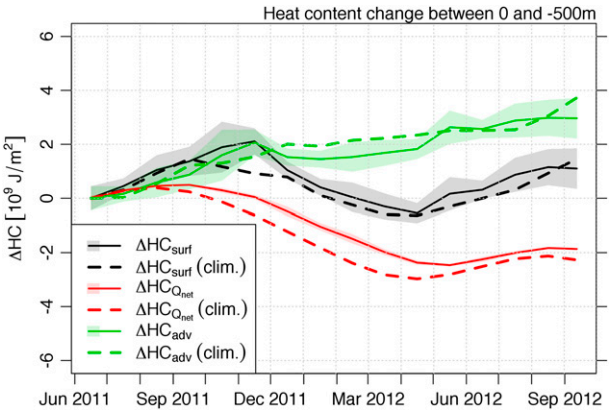

FIG. 8. Change in surface heat content at the mooring (relative to the start of the record) for the 2011 data (black), heat input from the atmosphere (red), and the inferred lateral advection of heat (green). The shaded regions indicate ±1 standard deviation from the monthly average. The dashed lines indicate the climatological values from the GINS hydrography (black), ERA-Interim (red), and the difference (green).

enter the region from along the east coast of Greenland and from the northward-flowing AW current along the western side of the Reykjanes Ridge (Fan et al. 2013).

To date, very few studies have explicitly examined anticyclones in the Lofoten basin. Using altimetry and a numerical model, Köhl (2007) verified the boundary current instability processes and further concluded that the shed anticyclones tend to merge in the deepest part of the Lofoten basin to form the Lofoten vortex (see also Poulain et al. 1996; Gascard and Mork 2008; Rossby et al. 2009a; Søiland and Rossby 2013). Rossby et al. (2009a) presented a section through such an anticyclone, highlighting large, downward isopycnal displacements (~400 m) and the large volume.

A gridded current field was created for the 2011 mooring by combining the eight Aquadopp current meters with the upward-looking ADCP and linearly interpolating to a 10-m grid (Fig. 9). In the mooring observations, the presence of eddies can be inferred by velocity variations on time scales of days to weeks, as well as by mooring blowdown caused by drag in strong currents (Fig. 5c). Note that in this section we focus only on the 2011 deployment (from May 2011 to September 2012) because of the lack of velocity measurements prior to this period. The u and v components have been low-pass filtered with a 5-day cutoff Butterworth filter to remove high-frequency fluctuations such as tides. In addition, longer time-scale background currents were removed by subtracting 4-month, cutoff, low-pass filtered fields. The variance in the eddy band is typically more than an order of magnitude larger than in the background, suggesting that eddy motions dominate the variability. The pulses of high velocity caused by eddies are intensified in the upper 1000 m; however, there is a barotropic signature to the flow that reaches to the deepest current meter (at 2500 m). The presence of an eddy over the mooring can be further demonstrated by plotting progressive vector diagrams (calculated from the unfiltered velocities) at various depths (Fig. 9c), which show looping patterns consistent with a passing vortex (Lilly and Rhines 2002). Note also the weak mean flow at depth, consistent with previous observations (Voet et al. 2010).

The presence of cyclonic or anticyclonic vortices can be inferred by examining the density anomaly, calculated relative to a mean vertical profile where the seasonal signal has been removed (Fig. 10). The deseasoned signal was calculated by removing the 4-month, cutoff, low-pass filtered time series for the upper 500 m and a time mean for depths greater than 500 m. In Fig. 10, deepening (shoaling) isopycnals imply anticyclonic (cyclonic) circulation. A set of 22 periods of deepening isopycnals were identified as possible anticyclones, and the temperature and salinity of the upper 300 m was calculated (Figs. 10b,c). An average over 0–300 m was chosen to emphasize the upper layer, where the signal of boundary current–sourced anticyclones should be the largest.

The average upper-ocean temperature and salinity anomalies within the inferred anticyclones are largely positive, with only a few periods of negative or near-zero anomaly (Figs. 10b,c). The maximum anomalies are 0.3°C and 0.02 psu (mean values of 0.14°C and 0.004 psu), which correspond to a maximum density decrease within anticyclones of approximately 0.04 kg m^{-3} (mean decrease of 0.015 kg m^{-3}). The magnitudes of the anomalies observed in the Lofoten basin are smaller than similar observations in the central Irminger Sea (Fan et al. 2013) and the Labrador Sea (e.g., de Jong et al. 2013).

a. Eddy model

To determine the properties of the eddies (including propagation direction and speed, radius, average temperature, and salinity), the mooring fields were fit to an idealized eddy model following the procedure of de Jong et al. (2013). First, the depth-averaged mooring velocities in the upper 500 m were regressed against the velocity field for a Rankine vortex rotated through various angles, with the azimuthal velocity given by

$$v_\theta(r) = \begin{cases} V_{\max}\dfrac{r}{R} & \text{for} \quad r < R \\ V_{\max}\dfrac{R}{r} & \text{for} \quad r > R, \end{cases} \tag{5}$$

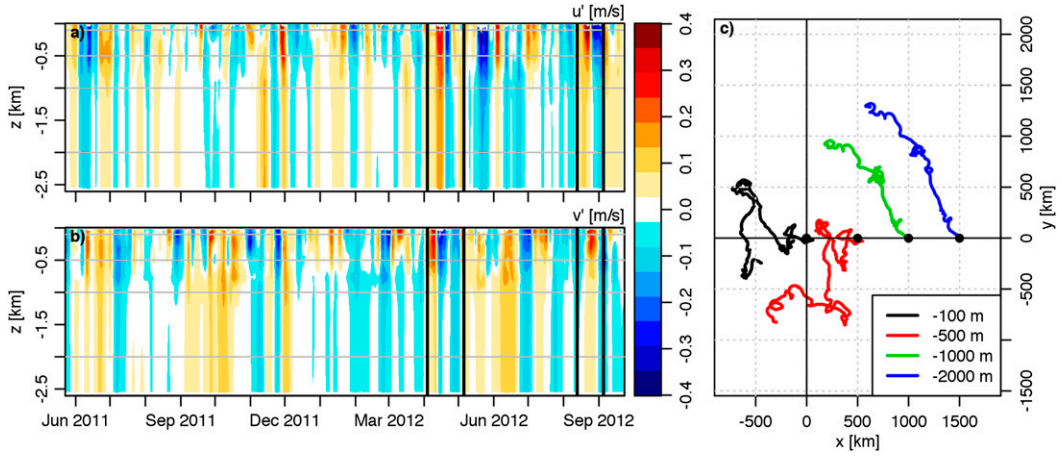

FIG. 9. Velocity anomalies (calculated by removing the seasonally filtered velocities) measured by the 2011 Aquadopps and ADCP in the (a) meridional and (b) zonal directions. The solid vertical lines indicate the eddy focus periods discussed in the text, and the gray horizontal lines indicate the depth for the progressive vector diagrams in (c). Note the origin in (c) is offset progressively by 500 km for each depth, and the progressive vectors are calculated using the unfiltered velocities.

where $V_{\max}$ is the maximum speed, which occurs at a radial distance r equal to the eddy radius R. The angle for which the highest correlation is found corresponds to the propagation direction α_e.

To determine the propagation speed, it is assumed the dynamic height calculated using the hydrographic measurements is a good proxy for the sea level anomaly (SLA). At high latitudes, the Rossby radius is of the same order or smaller than the separation between satellite altimeter tracks, making the gridded SLA maps useful only for measuring the largest eddies. De Jong et al. (2013) found good correlation between dynamic height and sea level anomaly for Irminger rings observed in the Labrador Sea, and we assume that the same relationship holds for the Lofoten basin. From geostrophy, the cross-stream eddy velocity V_c in a frame of reference rotated in the propagation direction is

$$V_c = \frac{g}{c_e f}\frac{dD}{dt}, \tag{6}$$

where c_e is the propagation speed, D is the dynamic height (relative to 2500 m), and the spatial gradient of D (e.g., dD/dx) has been converted to a time derivative through $dx = c_e dt$. Matching the velocity peaks on either side of the eddy core with the velocity estimated from the dynamic height gradient gives two estimates of the propagation speed, permitting an estimate of the uncertainty (estimated as half the difference). Once c_e is obtained, the time coordinate can be converted to a spatial coordinate and the radius estimated from the locations of the two azimuthal velocity peaks.

The above analysis assumes that the eddy passed nearly directly over the mooring; however, if there is an offset between the path of the center of the eddy and the mooring, the estimate of the radius will be too small. As discussed in de Jong et al. (2013), however, unless the eddy merely grazed the mooring (in which two distinct velocity maxima would not be observed), the maximum correction is approximately 25% (based on an offset of $\frac{3}{4}R$).

Of the 22 features identified in Fig. 10, only six fit the eddy model based on the assumed shape of the density and velocity fields (Table 1). Of the six eddies, the mean radius was 17.4 ± 9.0 km, the mean propagation speed was 6.0 ± 2.9 cm s^{-1}, and the mean $V_{\max}$ was 21.5 ± 9.4 cm s^{-1} (calculated as an average over the upper 500 m). The uncertainties represent the standard deviation of the individual estimates. Of the six eddies, three were observed to be propagating toward the north-northeast (eddies 3, 14, and 20), while the other three were propagating to the south-southwest (eddies 4, 13, and 21). Eddies 20 and 21 have very similar properties but nearly opposite propagation direction and may in fact be two observations of the same eddy, which turned and encountered the mooring a second time.

In the following sections, we focus on two specific eddies: a large mode-water eddy observed in April 2012 and an energetic anticyclone observed during August 2012.

b. *April 2012 eddy*

The largest deepening of isopycnals, occurring around 18 April 2012 (eddy 14 in Fig. 10), corresponded to a

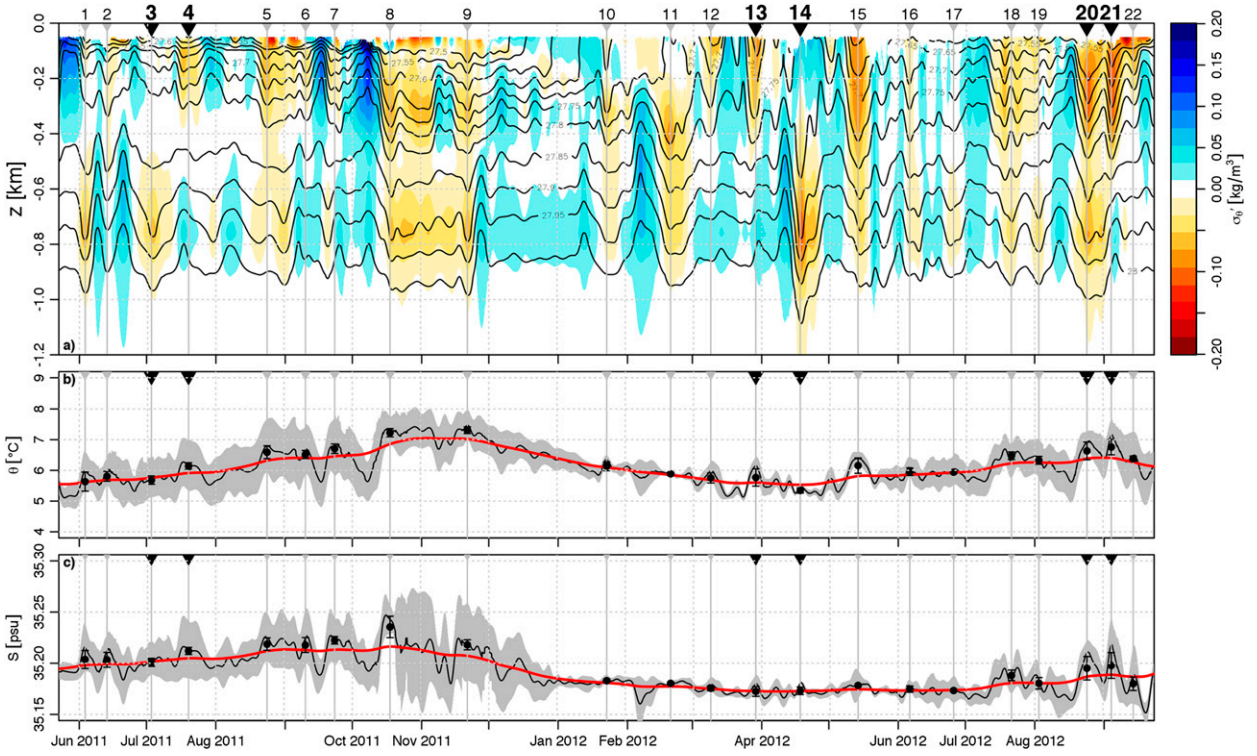

FIG. 10. (a) Density anomalies calculated from the gridded 2011 hydrography, with isopycnals overlain (contour interval of 0.05 kg m^{-3}). The triangles and vertical lines indicate times of inferred anticyclonic eddies, where the black triangles indicate eddies fit using the model described in section 4a. (b) Potential temperature of the upper 300 m (black), with the seasonal signal in red, and (c) salinity of the upper 300 m with the seasonal signal. In (b) and (c), the gray regions highlight ±1 standard deviation of the vertical average, and the points show the time-averaged, near-surface potential temperature and salinity within each of the inferred anticyclones, with error bars for plus/minus one standard deviation of the eddy average.

positive density anomaly between the surface and 300 m and a negative anomaly deeper than 300 m. Before and after this time, the mooring experienced significant blowdown from strong currents (see Fig. 5c). The strong currents and the downward heaving of isopycnals are consistent with an anticyclonic vortex (e.g., Lilly and Rhines 2002; de Jong et al. 2013).

For the April 2012 eddy, the propagation direction was determined to be 76° (counterclockwise from the east, corresponding to 14° clockwise from the north). The propagation speed c_e was estimated to be 11 ± 1 cm s^{-1}, the maximum velocity V_{max} = 33 ± 5 cm s^{-1}, and the radius R = 32 ± 3 km. The April anticyclone is unique in the record in that the core of the eddy is composed almost exclusively of mode water (discussed below).

To estimate the total volume of the eddy, we examined isopycnal layer thicknesses in the density range of the core of the eddy. It was found that the maximum thickness anomaly occurred between the 27.76 and 27.8 kg m^{-3} isopycnals, with a maximum value of approximately 450 m (compared to the mean thickness of 128 m). The increasing thickness in this layer is the result of an anomalous volume of fluid of the same density, which causes upward heaving of isopycnals for the 27.76 kg m^{-3} isopycnal and depression of the 27.8 kg m^{-3} isopycnal. A second, smaller volume anomaly follows the passage of the eddy. Whether this second feature represents another anticyclone or the same eddy passing back over the mooring at a farther distance from the center is unclear. To isolate only the first feature, the shape of the left-hand side (i.e., approaching side) of the eddy was fit with a Gaussian profile. The volume was then determined by integrating the thickness anomaly profile, assuming radial symmetry, to give an eddy volume of $V_e = 2.0 \times 10^{12}$ m^3. This volume is similar to one estimated by Rossby et al. (2009a) (1.5×10^{12} m^3) from a chance hydrographic section through a large anticyclone in the Lofoten basin in July 2000 (estimated eddy height of 300 m and radius of 40 km). The average temperature and salinity of the eddy core was determined to be 5.28° ± 0.06°C and 35.17 ± 0.01 psu, where the uncertainties represent the standard deviations.

The temperature and salinity of the eddy core are consistent with mixed layer properties for the same time

TABLE 1. Summary of eddy properties fit using the method described in section 4. The numbers in column 1 refer to the labeling in Fig. 10. Angles for α_e are in degrees counterclockwise from east.

Eddy	Date	R (km)	c_e (m s^{-1})	V_{max} (m s^{-1})	α_e	$\overline{\theta_e}$ (°C)	$\overline{S_e}$
3	3 Jul 2011	16 ± 2	0.06 ± 0.01	0.17 ± 0.01	43°	5.68	35.20
4	19 Jul 2011	8 ± 5	0.04 ± 0.02	0.12 ± 0.00	227°	6.14	35.21
13	31 Mar 2012	25 ± 3	0.07 ± 0.01	0.14 ± 0.01	226°	5.77	35.17
14	18 Apr 2012	32 ± 3	0.11 ± 0.01	0.33 ± 0.05	76°	5.35	35.17
20	25 Aug 2012	12 ± 1	0.06 ± 0.01	0.33 ± 0.02	91°	6.63	35.20
21	5 Sep 2012	13 ± 4	0.06 ± 0.01	0.20 ± 0.02	281°	6.76	35.20
Average		17 ± 9	0.06 ± 0.03	0.22 ± 0.09		6.04	35.19

of year, indicating that the eddy is composed of mode water. In isopycnal coordinates, the temperature and salinity of the 27.76 to 27.8 kg m^{-3} layer have slight anomalies relative to the background (Fig. 11c). The maximum magnitude of the isopycnal temperature anomaly is approximately 0.15°C, while the isopycnal salinity anomaly is ~0.01 psu (not shown).

c. *August 2012 eddy*

The second eddy to be focused on passed the mooring around 25 August 2012 (eddy 20 in Fig. 10) during a period of high, near-surface stratification (Fig. 5). Unlike the April eddy, the August eddy did not contain mode water and exhibited downward heaving of isopycnals at all depths (Fig. 12). The radius was found to be less than half of the April eddy, at 12 ± 1 km, with a propagation direction of 91° (i.e., North) and propagation speed of 6 ± 1 cm s^{-1}. The speed V_{max} was found to be 33 ± 2 cm s^{-1}.

As the August eddy is not clearly delineated by an isopycnal layer, we calculate the volume using a cylinder with a radius of 1.5R, based on the fact that the warm, saline core of the eddy extends beyond the radius of maximum velocity (e.g., Hátún et al. 2007; de Jong et al. 2013). The bottom extent of the eddy is taken to be the average depth of the σ_θ = 27.8 kg m^{-3} isopycnal (~450 m), giving a volume of 0.19 × 10^{12} m^3, approximately a tenth of the volume of the April eddy. The average temperature and salinity of the eddy are 6.76° ± 0.49°C and 35.20 ± 0.02 psu, respectively.

d. *Eddy anomalies and source water properties*

In this section, we examine the properties of the April and August eddy properties in the context of their source region, that is, the NwAC along the Lofoten slope.

The April eddy was observed at the end of the period of wintertime heat loss, and here we consider the lifetime of the eddy and its associated water properties relative to the observed mixed layer properties. The northward propagation direction is consistent with previous estimates of eddy motion at the mooring location by Volkov et al. (2013), and it suggests that the eddy did not travel directly from the slope current region straight to the mooring.

Next, we consider the boundary current properties, that is, the source water for the anticyclones. The boundary current water properties for spring 2012 were estimated from archived CTD profiles acquired in the region (H. Søiland 2013, personal communication). Averaged potential temperature and salinity between the 27.7 kg m^{-3} isopycnal and 100-m depth are shown in Fig. 13 for profiles available in the slope current region (error bars indicate plus/minus one standard deviation of the profiles over the specified depth range). The April and August 2012 eddy properties are plotted at the time of their passing. Note that no CTD data are available from about October 2011 to February 2012. Salinity within the slope current varies by ~0.05 around the average of 35.16 psu, which is consistent with the values observed in both the April and August eddies (35.17 and 35.20 psu, respectively), supporting the hypotheses that they contain slope current–sourced water, given that there are no other significant sources of high-salinity water in the region.

The average slope current temperature was warmer than the April eddy temperature by approximately 1.5°C during March and April 2012 (Fig. 13a). Given that the warmest slope current temperatures typically occur around December, the actual eddy–source water temperature difference may be even larger. This implies that the eddy was long lived enough to have lost at least 1.5°C to the atmosphere, consistent with the mixed layer heat lost during winter 2011. The positive isopycnal temperature (and salinity) anomaly within the April eddy suggests that the eddy was sourced from the boundary current but also that it was likely formed after the winter cooling period began.

The inset TS diagram in Fig. 13c highlights the differences between the 2011 mixed layer properties and those of the slope current water from CTD measurements. In particular, the TS properties of the April eddy (indicated with the diamond) are nearly identical to the mixed layer properties at the end of the cooling season (see Fig. 6), indicating that wintertime ventilation of the

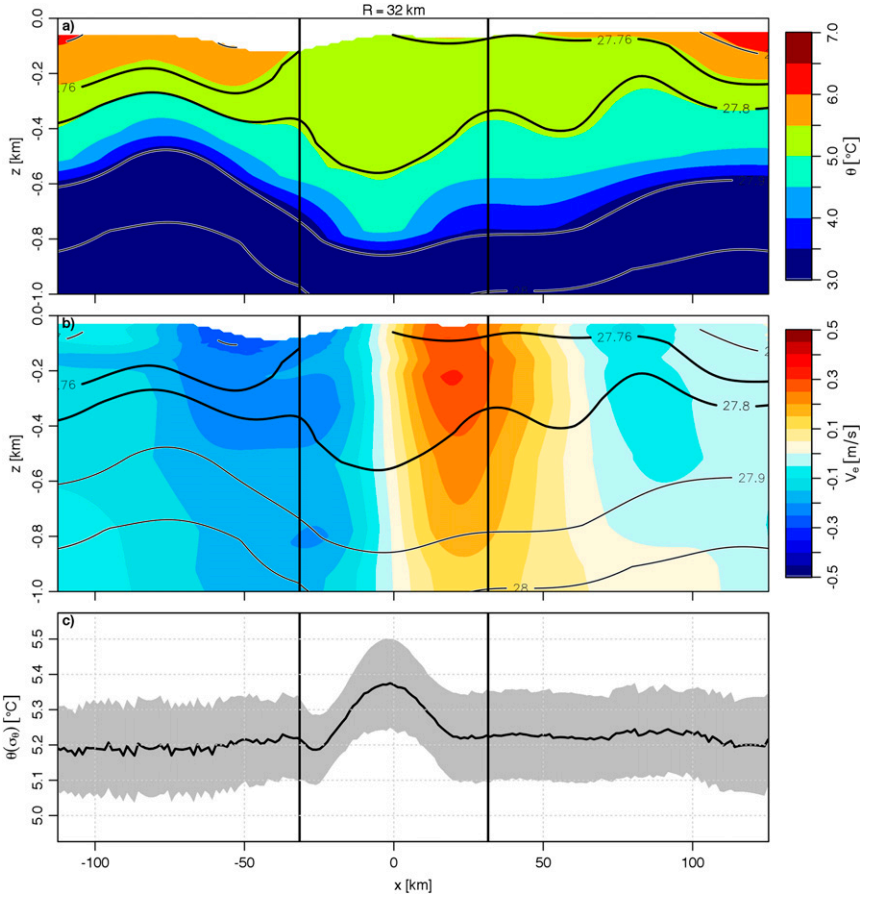

FIG. 11. Details of the April 2012 eddy. (a) Potential temperature, with contours of the density field and the 27.76 and 27.8 kg m^{-3} isopycnals (thick black lines) and (b) azimuthal eddy velocities. (c) The average temperature of the isopycnal layer ±1 standard deviation. The vertical bars indicate the estimate of the eddy diameter (R = 32 km). The x coordinate is constructed from the time series using the inferred propagation speed c_e.

eddy is likely responsible for the observed properties at the mooring location. Given the similarities between the eddy water mass and the mixed layer properties, a rough estimate of the eddy lifetime suggests that it is slightly less than the winter cooling period. Because such an estimate is based on the observed water properties, it is not possible to determine conclusively that the eddy existed as a coherent entity for the entire time, as it may have undergone breakup or mergers with other anticyclones in the basin. Conversely, the TS properties of the August eddy are consistent with the slope current properties, indicating that it is a relatively young eddy.

5. Discussion

a. Eddy anomalies

Unlike anticyclonic eddies found in other high-latitude seas, such as the Labrador Sea, the Lofoten basin anticyclones observed in the mooring record do not exhibit large temperature and salinity anomalies relative to the background (Fig. 10). In the Labrador Sea, de Jong et al. (2013) observed warm-core anticyclones propagating toward the recently ventilated central Labrador Sea, with surface temperatures 2°–3°C greater and salinities ~0.1 psu greater than the average Labrador Seawater (LSW) values. In the Irminger Sea, anticyclones observed from a mooring by Fan et al. (2013) were also seen to contain anomalously warm and salty water, with mean anomalies relative to the non-eddy background of approximately 0.28°C and 0.03 psu. The small anomalies in the Lofoten basin (approximately half the Irminger Sea and an order of magnitude smaller than the Labrador Sea) are likely at least partially due to the size of the basin and that the topography ensures that anticyclones will be confined to it, thus creating the characteristic ''deep pool'' of warm and salty water (e.g., Figs. 2, 3).

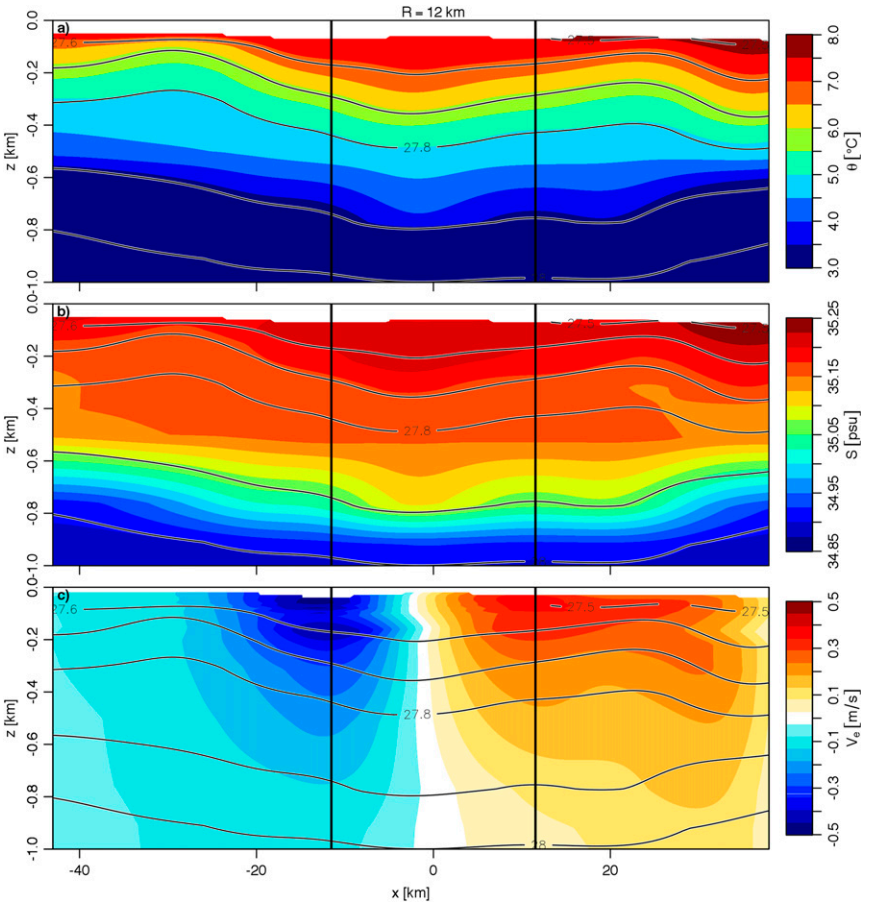

FIG. 12. Details of the August 2012 eddy. (a) Potential temperature, (b) salinity, and (c) azimuthal eddy velocities, overlain with contours of the density field. The vertical bars indicate the estimate of the eddy diameter (R = 12 km). The x coordinate is constructed from the time series using the inferred propagation speed c_e.

It is clear from the one-dimensional heat budget at the mooring that lateral transport is significant (Fig. 8); however, quantifying fluxes from observations is a challenge. From the chance observation of a warm anticyclone (approximate radius of 40 km), Rossby et al. (2009a) speculated that approximately 24 such eddies would be required to balance the net annual heat loss in the Lofoten basin, assuming that they balance a 2°C drop in temperature averaged over the basin. Results from the present study suggest that the average eddy size is smaller than 40 km, indicating that the required number of eddies could be much larger. The small anomalies between eddies and the ''noneddy'' background suggest that the mean state of the basin is continually fed by eddies, which in turn suggests a rapid and efficient exchange with the boundary current. Despite increased knowledge of the structure and dynamics of the Lofoten basin anticyclones, an estimate of the flux required to balance surface cooling remains crude and further attempts at refinement will need to be made using additional data and tools.

Given that the slope current water properties vary seasonally (Fig. 13), the hydrographic properties of eddies observed in the basin might be expected to vary similarly, with a lag. No evidence of this delayed seasonal cycle was observed in the mooring, where the warmest eddies were observed during December, when the slope current temperatures are expected to be warmest. The absence of a clear lag between the slope current and the mooring was perhaps because of the location of the mooring relative to the mean pattern of eddy propagation (Volkov et al. 2013), where the seasonal signal associated with shedding from the boundary current is erased by the transformation of eddies within the basin and perhaps also indicative of a rapid and efficient exchange with the NwAC.

In addition to the seasonal variation in properties, previous studies have suggested that the baroclinic

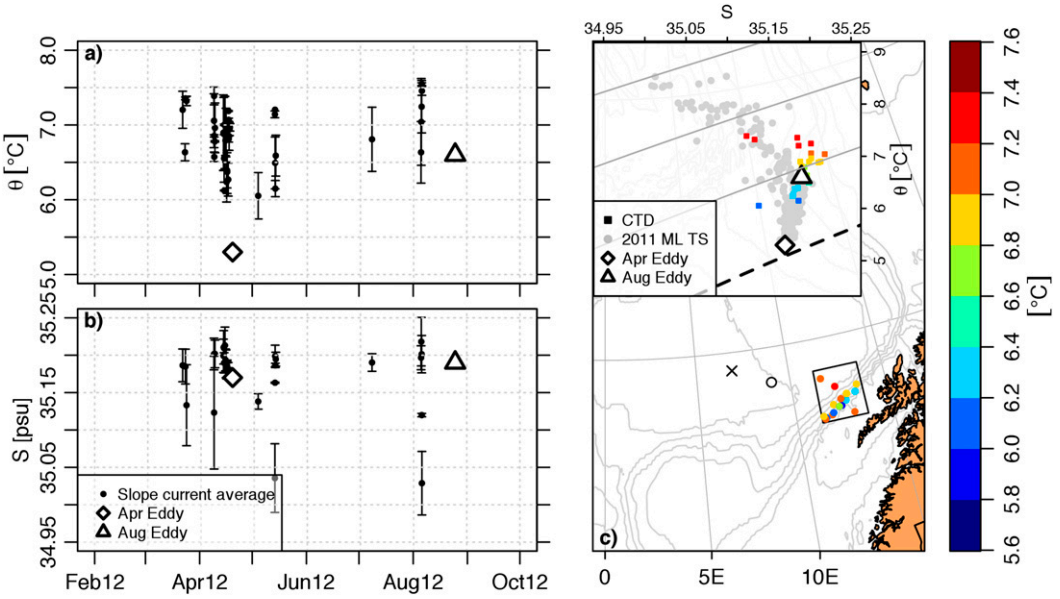

FIG. 13. Properties of the slope current region in 2012, vertically averaged between the 27.7 kg m^{-3} isopycnal and 100-m depth. (a) Potential temperature of the slope current from CTDs (points), the April eddy (diamond), and the August eddy (triangle). The error bars indicate plus/minus one standard deviation of the averages. (b) As in (a), but for salinity. (c) Map showing the averaging region, with each CTD profile location plotted as a point colored by the mean temperature. The × indicates the location of the mooring, and the ∘ indicates the location of the anticyclone discussed in Rossby et al. (2009a). The inset shows the TS properties of the boundary current averages (colored squares), plotted with the 2011 mixed layer properties. The two eddy TS properties are indicated by the diamond and the triangle.

instability process responsible for eddy generation will be more intense in the winter because of steeper isopycnal slopes and larger baroclinic transport (see, e.g., Spall 2010). Using two observational datasets and a numerical model, Isachsen et al. (2012) assessed eddy heat flux convergence in the eastern Nordic Seas and found the largest values in the Lofoten slope region. Averaged by season, they found that the depth-integrated flux convergences along the NwAC are larger in winter (November–April) than in summer (May–October) and that approximately half of the cooling of the NwAC was due to heat flux divergence along the Lofoten slope.

While 2 yr of data are not sufficient for assessing seasonal variation, it is possible to use mooring blowdown as a proxy for eddy encounters. Figure 5c shows the time series of pressure for the MicroCAT at 100-m depth, at the flotation sphere, which appears to support the notion that the eddy field is more energetic in the winter months. However, the character of the blowdown in winter 2010 is different from winter 2011, with the latter showing a handful of large events rather than a continuous buffeting by currents. Variation in horizontal eddy fluxes from one year to the next may be responsible for the interannual temperature and salinity variation observed in the 2-yr record—that is, an anomalously large eddy flux during a year of favorable generation conditions may ''overfill'' the basin with heat and salt, which will diffuse out of the region much more slowly, either through exchange with seas to the west or upward mixing of cold freshwater from below. A recent estimate of the long-term freshwater budget for the entire Norwegian Sea shows a freshening of about 0.007 psu $decade^{-1}$, though the trend from about 1995 to 2010 is opposite the long-term trend at about -0.012 psu yr^{-1} (Mork et al. 2014, their Fig. 2). Longer time series are needed to better characterize the long-term heat and salt budgets of the Lofoten basin and the connection with eddy fluxes.

The observation that the water temperature–salinity properties of the April eddy are nearly identical to the mode-water properties at the mooring suggests that in winter the eddies themselves may be important locations for mode-water formation and heat loss.

b. *Comparison of the Lofoten basin and Labrador Sea*

The mooring measurements discussed thus far reveal the seasonal water mass transformation process

and suggest that the influence of the lateral fluxes due to anticyclones is enhanced in the Lofoten basin. Qualitatively, the dynamics in the Lofoten basin are similar to the Labrador Sea, another location of significant mode-water formation and a region that has been intensely studied over the last several decades. To frame the present results in the context of the broader MOC, in this section we compare properties of the Lofoten basin with those inferred for the Labrador Sea, with a particular focus on the buoyancy loss through surface processes and the magnitude of the lateral eddy fluxes.

Given that both the Lofoten basin and Labrador Sea are regions of intense wintertime surface buoyancy flux and mode-water formation, it is expected that at least some of the relevant dynamics will be common between the two systems. There are, however, significant differences inherent the two regions, including an overall warmer and saltier boundary current water in the Lofoten basin, as well as the lack of a fully cyclonic boundary current; topographic blocking of the deep waters in the Nordic Seas by the Greenland–Scotland Ridge, resulting in a cold–fresh deep layer in the Lofoten basin (as opposed to a cold–salty layer in the Labrador Sea); and a stronger density contrast between the boundary current and interior water in the Lofoten basin (discussed below).

From the annually averaged buoyancy flux over the two basins and the total area, the annual surface buoyancy loss can be estimated. An estimate of the annually averaged buoyancy flux from the Bravo station in the center of the Labrador Sea is approximately -1×10^{-8} (Sathiyamoorthy and Moore 2002) versus $\sim -2 \times 10^{-8}\,\mathrm{m^2\,s^{-3}}$ for the Lofoten basin (Fig. 4b). Assuming an area with radius 230 km for the Labrador Sea (which is approximately the radius of the 3000-m isobaths; e.g., Straneo 2006b) and 150 km for the Lofoten basin, the annually averaged buoyancy loss is similar for the two basins (5.2×10^{10} vs $4.5 \times 10^{10}\,\mathrm{m^4\,s^{-3}}$ for the Labrador Sea and Lofoten basin, respectively). Assuming that contributions from the mean flow are small, if the surface buoyancy loss is to be balanced by the lateral input of buoyancy from eddy fluxes, the smaller perimeter of the Lofoten basin indicates that the lateral fluxes per unit length of the boundary current must be larger there.

In a simple, two-layer model of the Labrador Sea, Straneo (2006b) demonstrated the relationship whereby exchange with the boundary current balances the formation of dense water through surface buoyancy fluxes in the center of the basin. Horizontal eddy fluxes were parameterized (per unit of boundary current length) in terms of the isopycnal slope between the interior and the boundary current as

$$\int_H \overline{u'\rho'}\, dz = \frac{2cg}{\rho_0 f L}(\Delta\rho \Delta h)^2, \tag{7}$$

where H is the total depth of the layer in which convection is occurring; L is the width of the boundary current; c is an efficiency parameter related to the topographic slope (see, e.g., Spall 2004, 2012); $\Delta\rho$ is the boundary current–interior density difference; and $\Delta h = D - h_2$ is the height difference of the dense layer, where D is the height of the mode-water column in the interior, and h_2 is the thickness of the denser layer in the boundary current [see Eq. (8) in Straneo 2006b]. Note that Eq. (7) depends on the square of the density difference between the layers as well as the square of the difference between the heights of the layers in the boundary current versus the interior. A similar formulation, that uses a slightly different depth definition for H, is described in Spall (2004). The boundary current–interior density difference in the Lofoten basin was estimated to be approximately $0.2\,\mathrm{kg\,m^{-3}}$ (based on the synoptic section in Fig. 3 and on the climatology) by averaging the densities within the layers defined by the 27.9 and $27.7\,\mathrm{kg\,m^{-3}}$ isopycnals (approximately the base of the AW layer and the separation between boundary current and mode water). Using the June 2002 section from Fig. 3, the other parameters were estimated as $D = 400$ m, $h_2 = 100$ m, and $L = 100$ km. The parameter c was estimated as 0.03, within the range specified by Spall and Chapman (1998), and was consistent with Straneo (2006b), yielding a flux per unit length of $0.21\,\mathrm{kg\,(m\,s)^{-1}}$. Compared with the flux of $0.036\,\mathrm{kg\,(m\,s)^{-1}}$ estimated by Straneo (2006b) (using $\Delta\rho = 0.05\,\mathrm{kg\,m^{-3}}$, $D = 1200$ m, $h_2 = 700$ m, $L = 100$ km, and $c = 0.03$), the parameterized eddy flux per unit length in the Lofoten basin is approximately 6 times larger than the Labrador Sea.

The larger estimated eddy flux in the Lofoten basin is due to the enhanced density difference and is consistent with the greater surface buoyancy flux observed there, though the exact magnitude of the difference in parameterized eddy flux between the two basins should be considered a rough estimate only. Seasonal differences in boundary current properties (such as density, depth, and velocity) will alter the result of Eq. (7) throughout the year—it is possible that the wintertime lateral eddy flux would be larger in the Labrador Sea due to the large depth of convection compared to the Lofoten basin (e.g., approximately 1500 vs 500 m). Such a difference highlights the upstream control of the sill in the Nordic Seas, a feature that is not present in the Labrador Sea (e.g., Iovino et al. 2008). Regardless, the larger inferred fluxes in the Lofoten basin highlight that at steady state, the length of the unstable boundary current required to balance surface losses should be shorter than in the

Labrador Sea. This is consistent with the fact that the AW boundary current only flows along the eastern side of the Lofoten basin (i.e., there is not a cyclonic boundary current), and the region of maximum instability is only 200–300 km in length (see, e.g., Isachsen et al. 2012). The larger fluxes in the Lofoten basin are also consistent with the observed "pooling" and reduced eddy anomalies as discussed in section 5a. Further work and observations to quantify the depth-integrated eddy flux are required.

The approximate evolution of water mass transformation in the Labrador Sea and Lofoten basin can be visualized by identifying regions on a TS diagram (Fig. 14). In the Lofoten basin, warm–salty AW [i.e., Lofoten slope current (LSC)] is transformed though surface heat loss to form mode water, at a density of about 27.8 kg m^{-3}. Further water mass modifications made downstream of the Lofoten basin produce the colder–fresher product found in the Denmark Strait overflow water (DSOW). In contrast, water from the IC forms the boundary current around the Labrador Sea, which produces a colder and fresher mode-water product in the form of LSW. In the Labrador Sea, there is also a significant amount of lateral buoyancy flux through freshwater transport by Irminger rings—a result of the freshwater "cap" that is often observed in the upper 200 m above the eddies (e.g., Hátún et al. 2007; Rykova et al. 2009; de Jong et al. 2013). The source of this freshwater is the West Greenland Current, which overlies the Irminger Current in the eastern Labrador Sea. A similar but smaller fresh coastal current exists along the coast of Norway, which may be a source of freshwater for the Lofoten basin. No indication of such freshwater layers were observed in the mooring record, though the freshening of the 2010 winter mixed layer during a period of net evaporation suggests the existence of lateral freshwater transport. It is possible that such a freshwater cap exists only above 50 m, which was the depth of the highest MicroCAT. It is also possible for winter convection to have mixed such a cap into the core of the eddy, as has been hypothesized in the Labrador Sea. More observations of boundary current anticyclones in the Lofoten basin are necessary to accurately describe their contributions to the heat and freshwater budgets.

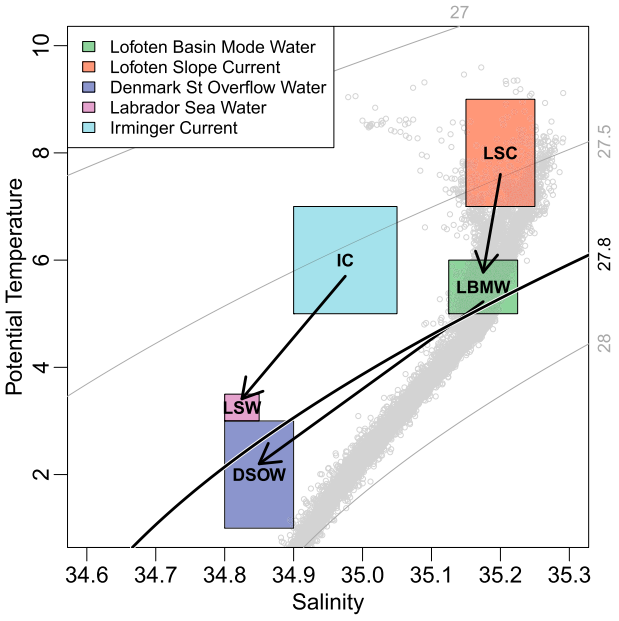

FIG. 14. Summary of TS properties in the Lofoten basin and in the Labrador Sea. Boxes represent approximate ranges for the identified water masses, and the gray dots are from the gridded 2011 MicroCATs.

6. Summary

In this study, 2 yr of hydrography and current measurements (from July 2010 to September 2012) from a mooring in the Lofoten basin of the Nordic Seas were analyzed to better understand the role of the Lofoten basin in water mass transformation as part of the MOC. The importance of the region is highlighted in the historical reanalysis data, from which it was determined that the Lofoten basin is responsible for approximately 1/3 of the total buoyancy loss despite having only 1/5 of the total area of the Nordic Seas (Fig. 4).

The hydrographic measurements reveal details of the winter water mass transformation and MLD evolution. Winter MLDs estimated for the 2 yr show a maximum extent of ~400 m, occurring around April, with shallower MLDs in 2011 than in 2010 (Fig. 5). To the first order, this difference is likely a result of interannual variation in the surface fluxes, with greater buoyancy loss in 2010 as well as an earlier and more abrupt start to the cooling period (Fig. 7). Accordingly, mixed layer properties differ between the 2 yr, with a maximum mixed layer density of 27.85 kg m^{-3} in 2010 and 27.79 kg m^{-3} in 2011 (Fig. 6)—similar to the minimum density of DSOW at ~27.8 kg m^{-3}. An analysis of the upper-ocean heat content at the mooring location suggests that lateral fluxes of ~80 W m^{-2} are required to balance the annually averaged heat loss (Fig. 8).

The lateral fluxes of heat and salt are believed to result from an energetic eddy field, originating along the Lofoten slope. Details of the eddy variability are revealed in the mooring data, through the current measurements and through isopycnal motion (Figs. 9, 10). Eddy motions are enhanced in the upper 1000 m but retain a barotropic signature to the bottom. Overall, the eddy anomalies are

small; mean potential temperature and salinity anomalies relative to the background are 0.14°C and 0.01 psu. What cannot be distinguished here is the extent that these anomalies represent recently formed eddies or eddies that have recirculated within the basin for some time. Of 22 potential anticyclones identified by the downward heaving of isopycnals, only 6 were able to be fit to an eddy model to extract eddy properties, giving an average radius, propagation speed, and maximum rotational velocity of approximately 17 km, 6 cm s^{-1}, and 22 cm s^{-1}, respectively.

Analysis of two of the eddies, in April and August 2012, reveals details of the eddy structures. The larger April eddy (R = 32 km) was found to be a mode-water eddy, suggesting that most of the original heat content at generation (possibly as much as 1°–2°C higher) was lost during its lifetime in the Lofoten basin. The August eddy (R = 12 km) had a clear temperature and salinity anomaly relative to the background and was of a temperature and salinity that was consistent with the slope current properties. Both eddies propagated approximately northward, consistent with previous estimates of eddy motions in the Lofoten basin (Volkov et al. 2013), rather than a direct path from the boundary current. The presence of a mode-water eddy suggests the potential for long lifetimes within the basin (e.g., similar to the cooling period) and that boundary-sourced anticyclones may be important locations for convection and water mass transformation.

The Lofoten basin is similar to the Labrador Sea in several regards, in that they are both regions of dense water formation bounded by warm–salty boundary currents. These two basins have similar buoyancy losses even though the Lofoten basin is smaller. Part of the reason is that a vigorous boundary–interior exchange is able to maintain a pool of warm water in the Lofoten basin, allowing for a large densification of the waters there. The larger eddy flux per unit length, because of the larger boundary current–interior density difference in the Lofoten basin, is consistent with the lack of a cyclonic boundary current and a shorter region of boundary current instability.

The mooring observations reveal the evolution of the mixed layer depth and properties during consecutive winters in 2010–12 and highlight previously unknown properties of the mesoscale anticyclonic eddy structure in the Lofoten basin. However, because of the point source nature of the mooring measurements, several questions remain to be answered. Beyond the individual events highlighted here, what are the basinwide characteristics of the eddy field (including seasonality)? How do the eddy heat–salt anomalies eventually add to the pool of buoyant water, and what roles do surface fluxes play in transforming eddies within the basin? To answer these questions more observations are required; however, the present paper provides a much-needed basis for such studies.

Acknowledgments. The authors thank M. Spall, H. Søiland, J. Lilly, T. Rossby, P. Gaube, and B. Harden for valuable discussions during the course of the study, and F. de Jong for assistance with the eddy fitting methods. Thanks also to J. Kemp, J. Ryder, and A. Ramsey for the mooring deployment as well as D. Torres, B. Hogue, and S. Worrilow for instrument preparation. Special thanks to H. Søiland for providing archived CTD data and for arranging the mooring deployment from the R/V *Håkon Mosby*. The work was supported by NSF OCE 0850416.

APPENDIX

MLD Estimates

A common approach to estimating ocean mixed layer depth is to use a temperature difference criterion, as described in section 1 and in KRH. Such an approach is well suited to data with large vertical spacing, such as standard oceanographic sampling depths, climatological averages, or fixed-depth sensors.

In contrast, when high-resolution vertical profiles are available [such as would be obtained from a CTD, XBT, expendable CTD (XCTD) or profiling float such as Argo], an estimate of the true depth of the mixed layer can be made much more accurately. If the vertical resolution is sufficient to resolve regions of high stratification, a gradient criterion may be employed where the MLD is defined as the depth at which $\partial\sigma_t/\partial z$ (or $\partial T/\partial z$) exceeds a threshold value, assuming there exists a sharp interface at the base of the mixed layer (see, e.g., KRH and references therein). In practice, a difference criterion is more commonly used than a gradient criterion, due in part to the limited vertical resolution of many historical and climatological data and based on the results of Brainerd and Gregg (1995), who found that MLDs based on a difference criterion were more stable than those based on a gradient criterion.

In a climatology of MLD over the global ocean using a database of ocean vertical profiles, de Boyer Montégut et al. (2004) use a temperature difference criterion similar to that of KRH but with a threshold value of ΔT = 0.2°C, based partly on a visual inspection of randomly sampled profiles and partly on comparison with several moored time series. They noted that the ΔT = 0.2°C criterion was successful at estimating not only the MLD but the springtime restratification following deep

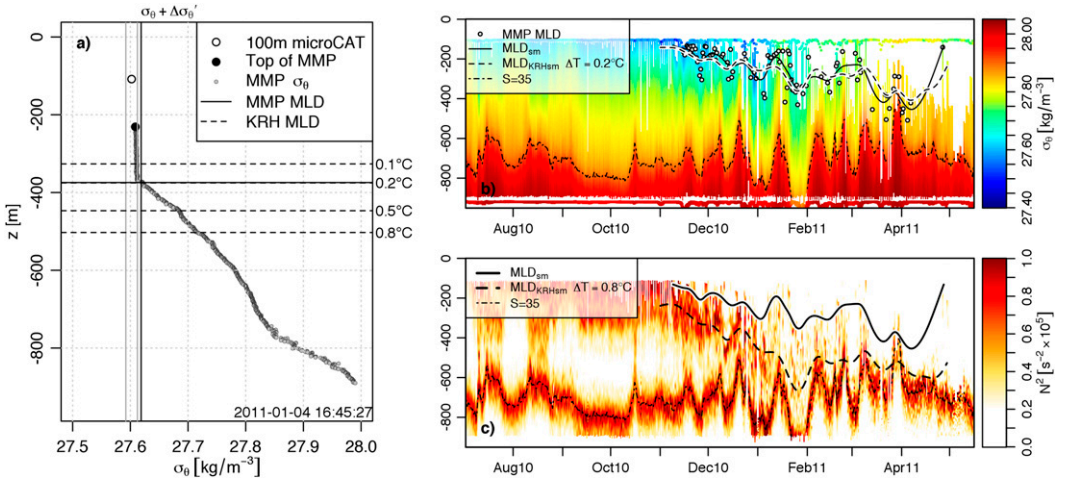

FIG. A1. Mixed layer depth estimate from the 2010 MMP profiles. (a) Example profile showing MLD estimate used in this study vs the method of KRH with various values of ΔT. (b) MMP σ_t field with raw (points) and smoothed (lines) MLD estimates. (c) MMP N^2 with MMP MLD (solid) and KRH method with $\Delta T = 0.8$°C (dashed).

winter mixed layers. Given the higher vertical resolution of the profiles used in their climatology compared to KRH, the smaller ΔT likely results in a MLD that is more consistent with a gradient criterion.

In the Nordic Seas, Nilsen and Falck (2006) estimated the MLD depth from water column profiles obtained at OWSM (66°N, 2°E) between the years 1949 and 1999. Because of the coarse vertical sampling of the OWSM profiles, Nilsen and Falck (2006) used the density difference criterion of KRH with a ΔT of 0.8°C, which they justified as having the highest success rate for finding the "pycnocline proper."

For the Lofoten mooring data, which differed between the 2 yr in terms of the vertical resolution of the profiles, the choice of mixed layer definition becomes complicated. On the one hand, the high resolution of the MMP profiles in 2010 permits an accurate estimate of the mixed layer depth but only when the mixed layer is deeper than 100 m (the highest extent of the water column measurements) and the profiler actually sampled a region of uniform density (relative to the value at ~100 m). Because of the previously discussed issues with the MMP not profiling all the way to the top float, especially from December 2010 onward, there are significant periods where the profiler did not climb high enough in the water column to observe the base of the mixed layer.

In contrast, when the mooring was turned around in May 2011, the MMP was replaced with fixed-depth MicroCATs, which provided high temporal sampling but coarse vertical resolution. Because of the 2011 resolution limitation, a difference criterion (with interpolation) is the only method suited to finding the MLD for that portion of the record. Such a method can also be applied to the MMP data, using the highest MicroCAT (~100-m depth) as the reference value.

As the goal in this study is to estimate the average properties (temperature, salinity, and density) of the winter mixed layer, a MLD definition that corresponds as close as possible to the actual base of the vertically homogeneous region is desired. This definition eliminates biases resulting from averaging colder and fresher water from the pycnocline below the actual mixed layer. Technically, such a definition is possible only with the 2010 MMP data and then only when the profiler actually sampled the homogeneous region. To construct a MLD estimate that can be applied to both the 2010 and 2011 data, an accurate but temporally inhomogeneous MLD was first estimated from the 2010 MMP profiles by defining a density difference $\Delta\sigma_t'$ and the MLD as the depth at which a change from a homogeneous layer of density σ_t to $\sigma_t + \Delta\sigma_t'$ occurs. To determine if the MMP actually sampled into such a layer, the topmost data point from the profile was compared with the value recorded by the 100-m MicroCAT, the latter having been interpolated to the same time as the MMP profile. If the absolute value of the difference in density recorded by the MicroCAT and the top of the MMP profile was within $\Delta\sigma_t'$, it was assumed that the MMP profiled into the mixed layer. Then, the depth in the MMP profile at which the density increased by $\Delta\sigma_t'$ (relative to the top of the profile) was located. Note that the MLD was found relative to the top of the profile rather than the MicroCAT because of slight variations between the measurements, possibly because of the interpolation of the MicroCAT

time series to the MMP times. It was found from visual inspection of profiles that a density difference of $\Delta\sigma_t' = 0.01\,\mathrm{kg\,m^{-3}}$ produced an accurate estimate of the base of the mixed layer.

Figure A1 shows an example MMP density profile (from 1645 UTC 4 January 2011), plotted with the topmost MicroCAT and the MLD inferred from the procedure described above. Also indicated are the MLDs inferred using the KRH method with values of $\Delta T = 0.1°, 0.2°, 0.5°$ and 0.8°C. Note that the KRH method with $\Delta T = 0.8$°C overestimates the depth of the base of the mixed layer in Fig. A1 by a factor of approximately 1.3. To find a value for the temperature difference that gives a MLD that is most consistent with that from the MMP density profiles, the KRH method was applied to the MMP data for $\Delta T = 0.1°$ to 1.0°C, and a linear regression of the two MLD estimates was calculated. The highest R^2 (0.94, $p < 2.2 \times 10^{-16}$, root-mean-square error of ~44 m) was found for $\Delta T = 0.2$°C, and a visual inspection of the inferred MLD plotted with the MMP density profiles confirmed that it produced a reasonable result (e.g., the regression with $\Delta T = 0.1$°C had a smaller rms error of 28 m, but it was found that the MLD was sometimes clearly too shallow).

REFERENCES

Andersson, M., K. A. Orvik, J. H. LaCasce, I. Koszalka, and C. Mauritzen, 2011: Variability of the Norwegian Atlantic Current and associated eddy field from surface drifters. *J. Geophys. Res.,* **116,** C08032, doi:10.1029/2011JC007078.

Brainerd, K. E., and M. C. Gregg, 1995: Surface mixed and mixing layer depths. *Deep-Sea Res. I,* **42,** 1521–1543, doi:10.1016/0967-0637(95)00068-H.

Chanut, J., B. Barnier, W. Large, L. Debreu, T. Penduff, J. Molines, and P. Mathiot, 2008: Mesoscale eddies in the Labrador Sea and their contribution to convection and restratification. *J. Phys. Oceanogr.,* **38,** 1617–1643, doi:10.1175/2008JPO3485.1.

Davis, X. J., F. Straneo, Y.-O. Kwon, K. A. Kelly, and J. M. Toole, 2013: Evolution and formation of North Atlantic Eighteen Degree Water in the Sargasso Sea from moored data. *Deep-Sea Res. II,* **91,** 11–24, doi:10.1016/j.dsr2.2013.02.024.

de Boyer Montégut, C., G. Madec, A. S. Fischer, A. Lazar, and D. Iudicone, 2004: Mixed layer depth over the global ocean: An examination of profile data and a profile-based climatology. *J. Geophys. Res.,* **109,** C12003, doi:10.1029/2004JC002378.

Dee, D. P., and Coauthors, 2011: The ERA-Interim reanalysis: Configuration and performance of the data assimilation system. *Quart. J. Roy. Meteor. Soc.,* **137,** 553–597, doi:10.1002/qj.828.

de Jong, M. F., A. S. Bower, and H. H. Furey, 2013: Two years of observations of warm-core anticyclones in the Labrador Sea and their seasonal cycle in heat and salt stratification. *J. Phys. Oceanogr.,* **44,** 427–444, doi:10.1175/JPO-D-13-070.1.

Deshayes, J., F. Straneo, and M. Spall, 2009: Mechanisms of variability in a convective basin. *J. Mar. Res.,* **67,** 273–303, doi:10.1357/002224009789954757.

Fan, X., U. Send, P. Testor, J. Karstensen, and P. Lherminier, 2013: Observations of Irminger Sea anticyclonic eddies. *J. Phys. Oceanogr.,* **43,** 805–823, doi:10.1175/JPO-D-11-0155.1.

Gascard, J.-C., and K. A. Mork, 2008: Climatic importance of large-scale and mesoscale circulation in the Lofoten basin deduced from Lagrangian observations. *Arctic–Subarctic Ocean Fluxes,* R. R. Dickson, J. Meincke, and P. Rhines, Eds., Springer, 131–143.

Gelderloos, R., C. Katsman, and S. Drijfhout, 2011: Assessing the roles of three eddy types in restratifying the Labrador Sea after deep convection. *J. Phys. Oceanogr.,* **41,** 2102–2119, doi:10.1175/JPO-D-11-054.1.

Gill, A. E., 1982: *Atmosphere–Ocean Dynamics.* International Geophysics Series, Vol. 30, Academic Press, 662 pp.

Hansen, B., and S. Østerhus, 2000: North Atlantic–Nordic Seas exchanges. *Prog. Oceanogr.,* **45,** 109–208, doi:10.1016/S0079-6611(99)00052-X.

Hátún, H., C. C. Eriksen, and P. B. Rhines, 2007: Buoyant eddies entering the Labrador Sea observed with gliders and altimetry. *J. Phys. Oceanogr.,* **37,** 2838–2854, doi:10.1175/2007JPO3567.1.

Iovino, D., F. Straneo, and M. Spall, 2008: On the effect of a sill on dense water formation in a marginal sea. *J. Mar. Res.,* **66,** 325–345, doi:10.1357/002224008786176016.

Isachsen, P. E., C. Mauritzen, and H. Svendsen, 2007: Dense water formation in the Nordic Seas diagnosed from sea surface buoyancy fluxes. *Deep-Sea Res. I,* **54,** 22–41, doi:10.1016/j.dsr.2006.09.008.

——, I. Koszalka, and J. H. LaCasce, 2012: Observed and modeled surface eddy heat fluxes in the eastern Nordic Seas. *J. Geophys. Res.,* **117,** C08020, doi:10.1029/2012JC007935.

——, M. Drivdal, S. Eastwood, Y. Gusdal, G. Noer, and Ø. Saetra, 2013: Observations of the ocean response to cold air outbreaks and polar lows over the Nordic Seas. *Geophys. Res. Lett.,* **40,** 3667–3671, doi:10.1002/grl.50705.

Jeansson, E., S. Jutterström, B. Rudels, L. G. Anderson, K. A. Olsson, E. P. Jones, W. M. Smethie Jr., and J. H. Swift, 2008: Sources to the East Greenland Current and its contribution to the Denmark Strait overflow. *Prog. Oceanogr.,* **78,** 12–28, doi:10.1016/j.pocean.2007.08.031.

Kara, A., P. Rochford, and H. Hurlburt, 2000: An optimal definition for ocean mixed layer depth. *J. Geophys. Res.,* **105,** 16 803–16 821, doi:10.1029/2000JC900072.

Köhl, A., 2007: Generation and stability of a quasi-permanent vortex in the Lofoten basin. *J. Phys. Oceanogr.,* **37,** 2637–2651, doi:10.1175/2007JPO3694.1.

Koszalka, I., J. LaCasce, and C. Mauritzen, 2013: In pursuit of anomalies—Analyzing the poleward transport of Atlantic Water with surface drifters. *Deep-Sea Res. II,* **85,** 96–108, doi:10.1016/j.dsr2.2012.07.035.

Lilly, J. M., and P. B. Rhines, 2002: Coherent eddies in the Labrador Sea observed from a mooring. *J. Phys. Oceanogr.,* **32,** 585–598, doi:10.1175/1520-0485(2002)032<0585:CEITLS>2.0.CO;2.

——, ——, M. Visbeck, R. Davis, J. R. N. Lazier, F. Schott, and D. Farmer, 1999: Observing deep convection in the Labrador Sea during winter 1994/95. *J. Phys. Oceanogr.,* **29,** 2065–2098, doi:10.1175/1520-0485(1999)029<2065:ODCITL>2.0.CO;2.

——, ——, F. Schott, K. Lavender, J. Lazier, U. Send, and E. D'Asaro, 2003: Observations of the Labrador Sea eddy field. *Prog. Oceanogr.,* **59,** 75–176, doi:10.1016/j.pocean.2003.08.013.

Martin, R., and G. W. K. Moore, 2007: Air-sea interaction associated with a Greenland reverse tip jet. *Geophys. Res. Lett.,* **34,** L24802, doi:10.1029/2007GL031093.

Mauritzen, C., 1996a: Production of dense overflow waters feeding the North Atlantic across the Greenland-Scotland Ridge. Part 1: Evidence for a revised circulation scheme. *Deep-Sea Res. I,* **43,** 769–806, doi:10.1016/0967-0637(96)00037-4.

——, 1996b: Production of dense overflow waters feeding the North Atlantic across the Greenland-Scotland Ridge. Part 2: An inverse model. *Deep-Sea Res. I,* **43,** 807–835, doi:10.1016/0967-0637(96)00038-6.

Moore, G. W. K., I. A. Renfrew, and R. S. Pickart, 2012: Spatial distribution of air-sea heat fluxes over the sub-polar North Atlantic Ocean. *Geophys. Res. Lett.,* **39,** L18806, doi:10.1029/2012GL053097.

Mork, K. A., and Ø. Skagseth, 2010: A quantitative description of the Norwegian Atlantic Current by combining altimetry and hydrography. *Ocean Sci.,* **6,** 901–911, doi:10.5194/os-6-901-2010.

——, ——, V. Ivshin, V. Ozhigin, S. L. Hughes, and H. Valdimarsson, 2014: Advective and atmospheric forced changes in heat and fresh water content in the Norwegian Sea, 1951–2010. *Geophys. Res. Lett.,* **41,** 6221–6228, doi:10.1002/2014GL061038.

Nilsen, J., and E. Falck, 2006: Variations of mixed layer properties in the Norwegian Sea for the period 1948–1999. *Prog. Oceanogr.,* **70,** 58–90, doi:10.1016/j.pocean.2006.03.014.

Orvik, K. A., Ø. Skagseth, and M. Mork, 2001: Atlantic inflow to the Nordic Seas: Current structure and volume fluxes from moored current meters, VM-ADCP and SeaSoar-CTD observations, 1995–1999. *Deep-Sea Res. I,* **48,** 937–957, doi:10.1016/S0967-0637(00)00038-8.

Pickard, G. L., and W. J. Emery, 1990: *Descriptive Physical Oceanography.* 5th ed. Butterworth-Heinemann, 320 pp.

Poulain, P., A. Warn-Varnas, and P. Niiler, 1996: Near-surface circulation of the Nordic Seas as measured by Lagrangian drifters. *J. Geophys. Res.,* **101,** 18 237–18 258, doi:10.1029/96JC00506.

Rossby, T., V. Ozhigin, V. Ivshin, and S. Bacon, 2009a: An isopycnal view of the Nordic Seas hydrography with focus on properties of the Lofoten basin. *Deep-Sea Res. I,* **56,** 1955–1971, doi:10.1016/j.dsr.2009.07.005.

——, M. D. Prater, and H. Søiland, 2009b: Pathways of inflow and dispersion of warm waters in the Nordic Seas. *J. Geophys. Res.,* **114,** C04011, doi:10.1029/2008JC005073.

Rykova, T., F. Straneo, J. Lilly, and I. Yashayaev, 2009: Irminger Current anticyclones in the Labrador Sea observed in the hydrographic record, 1990–2004. *J. Mar. Res.,* **67,** 361–384, doi:10.1357/002224009789954739.

Sathiyamoorthy, S., and G. Moore, 2002: Buoyancy flux at Ocean Weather Station Bravo. *J. Phys. Oceanogr.,* **32,** 458–474, doi:10.1175/1520-0485(2002)032<0458:BFAOWS>2.0.CO;2.

Seidov, D., O. Baranova, M. Biddle, T. Boyer, D. Johnson, A. Mishonov, C. Paver, and M. Zweng, 2013: Greenland-Iceland-Norwegian Seas regional climatology. NOAA/NODC, accessed 18 September 2013, doi:10.7289/V5GT5K30.

——, and Coauthors, 2014: Oceanography north of 60°N from World Ocean Database. *Prog. Oceanogr.,* **132,** 153–173, doi:10.1016/j.pocean.2014.02.003.

Skagseth, Ø., and K. A. Mork, 2012: Heat content in the Norwegian Sea, 1995–2010. *ICES J. Mar. Sci.,* **69,** 826–832, doi:10.1093/icesjms/fss026.

Søiland, H., and T. Rossby, 2013: On the structure of the Lofoten basin eddy. *J. Geophys. Res. Oceans,* **118,** 4201–4212, doi:10.1002/jgrc.20301.

——, M. Prater, and T. Rossby, 2008: Rigid topographic control of currents in the Nordic Seas. *Geophys. Res. Lett.,* **35,** L18607, doi:10.1029/2008GL034846.

Spall, M. A., 2004: Boundary currents and watermass transformation in marginal seas. *J. Phys. Oceanogr.,* **34,** 1197–1213, doi:10.1175/1520-0485(2004)034<1197:BCAWTI>2.0.CO;2.

——, 2005: Buoyancy-forced circulations in shallow marginal seas. *J. Mar. Res.,* **63,** 729–752, doi:10.1357/0022240054663204.

——, 2010: Non-local topographic influences on deep convection: An idealized model for the Nordic Seas. *Ocean Modell.,* **32,** 72–85, doi:10.1016/j.ocemod.2009.10.009.

——, 2011: On the role of eddies and surface forcing in the heat transport and overturning circulation in marginal seas. *J. Climate,* **24,** 4844–4858, doi:10.1175/2011JCLI4130.1.

——, 2012: Influences of precipitation on water mass transformation and deep convection. *J. Phys. Oceanogr.,* **42,** 1684–1700, doi:10.1175/JPO-D-11-0230.1.

——, and D. C. Chapman, 1998: On the efficiency of baroclinic eddy heat transport across narrow fronts. *J. Phys. Oceanogr.,* **28,** 2275–2287, doi:10.1175/1520-0485(1998)028<2275:OTEOBE>2.0.CO;2.

Straneo, F., 2006a: Heat and freshwater transport through the central Labrador Sea. *J. Phys. Oceanogr.,* **36,** 606–628, doi:10.1175/JPO2875.1.

——, 2006b: On the connection between dense water formation, overturning, and poleward heat transport in a convective basin. *J. Phys. Oceanogr.,* **36,** 1822–1840, doi:10.1175/JPO2932.1.

Voet, G., D. Quadfasel, K. Mork, and H. Søiland, 2010: The mid-depth circulation of the Nordic Seas derived from profiling float observations. *Tellus,* **62A,** 516–529, doi:10.1111/j.1600-0870.2010.00444.x.

Volkov, D. L., T. V. Belonenko, and V. R. Foux, 2013: Puzzling over the dynamics of the Lofoten basin—A sub-Arctic hot spot of ocean variability. *Geophys. Res. Lett.,* **40,** 738–743, doi:10.1002/grl.50126.